CHALMERS
UNIVERSITY OF TECHNOLOGY

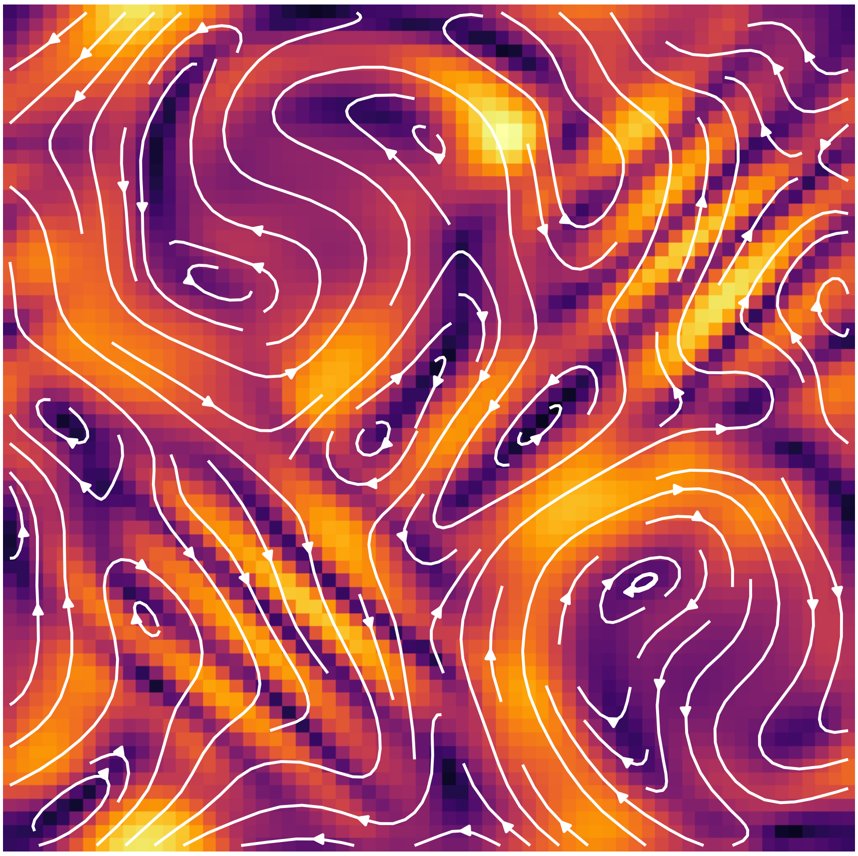

From Magnetic Field Seed Generation to Dynamo in Collisionless Plasmas

Thesis for the degree of Master of Science in Physics

LISE HANEBRING

DEPARTMENT OF PHYSICS

CHALMERS UNIVERSITY OF TECHNOLOGY
Gothenburg, Sweden 2025
www.chalmers.se

MASTER'S THESIS 2025

From Magnetic Field Seed Generation to Dynamo in Collisionless Plasmas

LISE HANEBRING

Department of Physics
Division of Subatomic, High Energy and Plasma Physics
Plasma Theory Research Group
CHALMERS UNIVERSITY OF TECHNOLOGY
Gothenburg, Sweden 2025

From Magnetic Field Seed Generation to Dynamo in Collisionless Plasmas
LISE HANEBRING

© LISE HANEBRING, 2025.

Supervisor: István Pusztai, Department of Physics
Examiner: István Pusztai, Department of Physics

Master's Thesis 2025
Department of Physics
Division of Subatomic, High Energy and Plasma Physics
Plasma Theory Research Group
Chalmers University of Technology
SE-412 96 Gothenburg
Sweden
Telephone +46 31 772 1000

Cover: A snapshot of the magnetic field strength and the projection of the magnetic field lines, for a cut of the three-dimensional simulation box, in a collisionless fluid dynamo simulation using the pressure isotropization closure.

Typeset in LaTeX
Gothenburg, Sweden 2025

From Magnetic Field Seed Generation to Dynamo in Collisionless Plasmas
LISE HANEBRING
Department of Physics
Chalmers University of Technology

Abstract

The origin of the cosmic magnetization present throughout the universe, greatly impacting the development of a diverse set of astrophysical systems, has long been a subject of research. Observations of cosmic magnetic fields, for example in the weakly collisional intracluster medium, show field magnitudes consistent with having been produced through the dynamo process, which causes small seed magnetic fields in plasmas to grow exponentially through the conversion to magnetic energy from kinetic energy in turbulent flows. Magnetohydrodynamics, the standard method of modeling dynamos, is not valid for weakly collisional systems since it assumes that a high collisionality dominates over competing small-scale processes, such as magnetic field seed-generating plasma instabilities. However, a fully kinetic treatment of the problem in electron-proton plasmas is prohibitively expensive numerically.

In this thesis an advanced collisionless fluid plasma model, with a complexity between that of magnetohydrodynamics and a kinetic model, is used to study magnetic field growth in a plasma in the presence of driven turbulent flows. A significant decoupling of the ion and electron dynamics is observed for the employed mass-ratio, allowing access to previously unexplored physics. The simulations demonstrate both the dynamo process and magnetic field seed generation through the electron Weibel instability. The fluid and magnetic Reynolds numbers, key quantities in classical dynamo theory, are generalized for a collisionless system. This is done by studying the dependence of flow and magnetic energy damping rates on the strength of the pressure isotropization encoded in the ion and electron heat flux closures of the fluid model. A scan over the effective magnetic Reynolds number is performed for the dynamo simulations by adjusting the strength of the electron closure. Strong pressure isotropization from the closure leads to behavior of the magnetic field growth expected from classical dynamo theory, whereas a small isotropization results in seed generation from pressure anisotropy-driven instabilities dominating, as previously observed in kinetic simulations of electron-positron plasmas.

Keywords: plasma, astrophysical dynamos, collisionless fluid models, Weibel instability.

Acknowledgements

First and foremost, I would like to express how grateful I am to have had the chance to work with everyone in the Plasma Theory Research Group at Chalmers for the last couple of years, as well as for the duration of this project. In particular I want to thank Tünde Fülöp, for giving me that opportunity and introducing me to plasma physics research, and my supervisor and examiner István Pusztai, for proposing such an interesting project and his invaluable guidance and feedback throughout. I am especially grateful to both of them for all their support in the first steps of my scientific career.

Furthermore, I am thankful for the support of James Juno at Princeton University, and to the rest of the developers of the 10-moment multifluid model of the Gkeyll code, without which the simulations in this thesis could not have been performed. The computations were enabled by resources provided by the National Academic Infrastructure for Supercomputing in Sweden (NAISS), partially funded by the Swedish Research Council through grant agreement no. 2022-06725.

Lastly, I am always grateful to my friends, and especially my family, for their encouragement and support.

Lise Hanebring, Gothenburg, June 2025

List of Acronyms

Below is the list of acronyms that have been used throughout this thesis listed in alphabetical order:

CFL	Courant-Friedrichs-Lewy
CGL	Chew-Goldberger-Low
GP	Galloway-Proctor
ICM	Intracluster medium
MHD	Magnetohydrodynamics
PIC	Particle-in-cell
RMS	Root-mean-square

Nomenclature

Below is a list of the variables and parameters that have been used throughout this thesis.

$\boldsymbol{E}$	Electric field
$\boldsymbol{B}$	Magnetic field
$\boldsymbol{b}$	Magnetic field unit vector
ϱ	Charge density
$\boldsymbol{j}$	Current density
$\alpha = e,\, i$	Species: electrons, ions
λ_{D}	Debye length
$\omega_{\mathrm{p},\alpha}$	Plasma frequency
δ_α	Skin depth
$\omega_{\mathrm{c},\alpha}$	Cyclotron frequency
$r_{\mathrm{L},\alpha}$	Larmor radius
$v_{\mathrm{th},\alpha}$	Thermal speed
μ	Magnetic moment
n_α	Number density
$\boldsymbol{u}_\alpha$	Fluid velocity
$\boldsymbol{\mathsf{p}}_\alpha$	Pressure tensor
$\boldsymbol{\mathsf{q}}_\alpha$	Heat flux tensor
p_α	Scalar pressure
T_α	Scalar temperature (in energy units corresponding to $k_B T_\alpha$)
ρ_{m}	MHD mass density
$\boldsymbol{U}$	MHD flow velocity
$\boldsymbol{\mathsf{p}}^*$	MHD pressure tensor
E_B	Magnetic energy density
E_U	MHD flow energy density

$\boldsymbol{U}_{\mathrm{GP}}$	Galloway-Proctor flow velocity
L_0	Characteristic system length scale
k_0	Characteristic system-scale wave number
u_0	Characteristic system-scale velocity fluctuation size
Rm	Magnetic Reynolds number
Re	Fluid Reynolds number
η	Resistivity
η_{m}	Magnetic diffusivity
ν	Kinematic viscosity
γ_B	Magnetic field damping rate
γ_U	MHD flow damping rate
$\mathit{\Delta}_\alpha$	Pressure anisotropy
$k_{\mathrm{w},\alpha}$	Most unstable Weibel mode (analytical)
$\gamma_{\mathrm{w},\alpha}$	Weibel magnetic field growth rate (analytical)
$k_{0,\alpha}$	Closure parameter
t_{turnover}	Turnover time
$t_{\mathrm{stream},i}$	Ion streaming time
M_0	Mach number
C_f	Force factor (dimensionless)

Contents

List of Figures

1

Introduction

Magnetic fields have long been known to permeate the universe, and have been observed in astrophysical systems of vastly different spatial scales — from planets and stars to galaxies and the intracluster medium (ICM) [1]. This magnetization is fundamental for the formation, evolution and structure of these systems. Observations for example show evidence of large-scale magnetic fields with spiral structures aligned with the spiral arms of galaxies [1]. How cosmic magnetization originated and how it has evolved, however, remains an open question, and is therefore an interesting topic of research.

Observed magnetic field strengths, structure and dynamics are consistent with them having been produced by, and being sustained by, the so called dynamo process [1]. This mechanism exponentially amplifies small "seed" magnetic fields in astrophysical plasmas (ionized gases) through the conversion of kinetic energy in turbulent flows to magnetic energy, saturating when the flow and magnetic energies reach equipartition. Its inherently multi-scale, three-dimensional nature poses a significant theoretical and computational challenge for dynamo modeling. The standard description of dynamos has therefore remained magnetohydrodynamics (MHD) [2], a relatively simple fluid plasma model. This model is valid in the collisional regime, and thus inaccurate for describing most astrophysical systems, like galaxies and the ICM, which are weakly collisional or almost completely collisionless on the scales of interest. Small-scale, kinetic processes like field-particle interactions, significant deviations from thermodynamic equilibrium and kinetic plasma instabilities dominate over the effects of collisions in such systems. Kinetic modeling — that is, resolving the full phase-space dynamics — would therefore be the most accurate treatment of collisionless dynamos. While important steps have been taken in this direction in recent years [3–5], these simulations face significant limitations due to excessive computational expense.

Collisionless fluid models [6] balance the computational efficiency of MHD with the higher physics fidelity of kinetic models, and thus constitute a useful alternative method for modeling astrophysical dynamos. This treatment considers velocity moment integrals of the governing statistical kinetic equation, so that certain velocity-space features of the particle distributions, like pressure anisotropy, are retained. It also allows kinetic effects, that are essential in collisionless systems, to be captured by a suitable closure relation (an "equation of state").

Since the dynamo process can only amplify an already present "seed" magnetic field, the origin of cosmic magnetization also relies on seed-generating mechanisms. Many such possible mechanisms have been investigated, but one of particular interest in collisionless astrophysical plasmas, where anisotropies naturally develop in the velocity distributions of the plasma particles, is the Weibel instability. This magnetic field seed-generating instability is pressure anisotropy-driven, and can generate fields of significantly larger strengths than other seed mechanisms [7]. Due to its fundamentally kinetic nature, the Weibel instability has not often been studied in the context of large-scale turbulent astrophysical systems like those relevant to dynamos.

In this thesis the aim is to study and characterize dynamos, as well as the role of the magnetic field seed-generating Weibel instability, when both the ions and the electrons in the plasma are modeled with collisionless fluid models. To accomplish this, the 10-moment collisionless fluid solver [8] of the `Gkeyll` plasma modeling framework [9, 10] is employed. This is one of the few such solvers that evolve the full fluid pressure tensors of both electrons and ions, making it possible to capture the effects of the Weibel instability in a non-kinetic setting. Three-dimensional simulations of driven turbulent flows are performed, allowing for both exponential amplification of magnetic fields through the dynamo process as well as seed generation through the Weibel instability. The magnetic and fluid Reynolds numbers, which are used to characterize dynamos in MHD studies, are generalized for a collisionless system by studying how magnetic field and flow damping rates in non-driven simulations scale with the strength of the two available closures of the fluid model. Having established its dependence on the closure strength, a scan over the effective magnetic Reynolds number is performed for the dynamo setup using the “isotropization closure”, that drives the system toward pressure isotropization, in order to compare the results with those of previous MHD dynamo simulations.

1.1 Outline

In chapter 2, the basic quantities and concepts of plasma physics, as well as MHD, fluid and kinetic plasma descriptions, are presented. Chapter 3 introduces the classical MHD description of dynamos, including the Reynolds numbers, and further discusses the problems with using MHD models for dynamos in the collisionless regime. This chapter also treats the magnetic field seed problem, introducing the Weibel instability, and demonstrates the possibility of using a collisionless fluid model to describe astrophysical dynamos. The simulation framework and the closures available in the used solver are also presented in chapter 3.

The simulation setup and results of the non-driven simulations of flow and magnetic field damping, used to generalize the Reynolds numbers for a collisionless system by scanning over closure strength, are presented and discussed in chapter 4. In chapter 5, the simulation setup and results of the scan over the effective magnetic Reynolds number for the dynamo simulations are presented. A more detailed analysis of the magnetic field growth thought to be associated with the Weibel instability is performed, and overall trends of the dynamo simulation scan are discussed, comparing the results to MHD dynamo studies. Finally, the conclusions drawn in this thesis are summarized in chapter 6.

2

Plasma Physics Theory and Descriptions

In this chapter some plasma physics concepts, quantities and description models are introduced as a background for treating the theory of the dynamo problem. The content of section 2.1 can be found for example in [11], while the content in sections 2.2–2.4 is based on [12] unless stated otherwise.

2.1 Fundamental Plasma Physics

Much of the visible matter in the universe is in the plasma state, the so called "fourth state of matter". One can imagine increasing the temperature of a gas enough for electrons to overcome the energy barrier binding them to atomic nuclei, ionizing the gas. In physical conditions that correspond to high enough ionization degrees, the resulting fluid state consists of neutral atoms as well as unbound electrons and ions. These interact primarily via electromagnetic forces due to the charged nature of the particles. A plasma is defined as such an ionized gas which displays *quasineutrality* and *collective behavior*.

Quasineutrality has to do with the property of ionized gases to screen charge irregularities at large enough distances through what is known as Debye shielding. Any charged particle placed in an otherwise charge neutral background of electrons and ions will induce an electric field that attracts oppositely charged particles and repels like-charged particles. The resulting particle displacement, which is dominated by electron motion at low timescales due to their lower inertia than that of ions, effectively shields the rest of the plasma from the test charge's electric potential at scales larger than the Debye length

$$\lambda_{\mathrm{D}} = \sqrt{\frac{\epsilon_0 T_e}{e^2 n_e}}. \tag{2.1}$$

Here e is the elementary charge, ϵ_0 the vacuum permittivity, and electron temperature and density are denoted by T_e and n_e respectively. Thus plasmas are approximately charge neutral — $\varrho \approx 0$, where ϱ is the charge density — at scales larger than λ_{D}. The quasineutrality condition for an ionized gas to be considered a plasma requires $\lambda_{\mathrm{D}} \ll L$, where L is the plasma scale, and $N_{\mathrm{D}} \gg 1$, where $N_{\mathrm{D}} = 4\pi n_e \lambda_{\mathrm{D}}^3/3$

is the number of electrons in a sphere of radius λ_D. The latter is required for a statistical description of the screening to be applicable.

The term collective behavior refers to the regime where particle motion is dominated by electromagnetic forces, rather than hard-sphere collisions. Since electromagnetic forces are long-range, it means that charged particles in a large region of the plasma affect each other's motion. The interaction is therefore non-local. Quantitatively the regime of collective behavior, where an ionized gas can be called a plasma, can be stated as $\omega_{\mathrm{p},e}/\nu > 1$. Here ν is the frequency of collisions with neutrals and, using the electron mass m_e,

$$\omega_{\mathrm{p},e} = \sqrt{\frac{e^2 n_e}{\epsilon_0 m_e}} \tag{2.2}$$

defines the (electron) plasma frequency — the frequency of typical electrostatic plasma oscillations due to small charge displacements. The ion plasma frequency is defined analogously using ion density, charge and mass. A related length scale that is commonly used in plasma physics is the skin depth, or inertial length, $\delta_\alpha = c/\omega_{\mathrm{p},\alpha}$ for the species index $\alpha = e,\ i$, where c is the light speed. This is the typical penetration depth of low frequency ($\omega \ll \omega_{\mathrm{p},\alpha}$) electromagnetic radiation in the plasma.

Because a plasma consists of charged particles, interaction is mediated via electric and magnetic fields. In a plasma with a magnetic field $\boldsymbol{B}$, charged particles are constrained to gyrate around the field lines in the plane perpendicular to $\boldsymbol{B}$ at the cyclotron frequency

$$\omega_{\mathrm{c},\alpha} = \frac{|q_\alpha| B}{m_\alpha} \tag{2.3}$$

where $B = |\boldsymbol{B}|$, and the mass and charge of the particle are m_α and q_α respectively. The radius of gyration is called the Larmor radius, or gyroradius, defined as

$$r_{\mathrm{L},\alpha} = \frac{v_{\perp,\alpha}}{\omega_{\mathrm{c},\alpha}} \tag{2.4}$$

where $v_{\perp,\alpha}$ is the velocity perpendicular to $\boldsymbol{B}$. To find a characteristic value for the Larmor radius one typically uses $v_{\perp,\alpha} \approx v_{\mathrm{th},\alpha}$, where the thermal speed is defined as

$$v_{\mathrm{th},\alpha} = \sqrt{\frac{2T_\alpha}{m_\alpha}}, \tag{2.5}$$

using the species temperature T_α. A plasma is said to be magnetized when the characteristic temporal and spatial scales on which plasma parameters vary are much larger than those of the particle gyration. If this is not true, the plasma is non-magnetized.

For a magnetized plasma where any variation of $\boldsymbol{B}$ is sufficiently slow (adiabatic), there are exponentially well conserved quantities for particles known as adiabatic invariants. The first of these is the magnetic moment

$$\mu = \frac{m v_\perp^2}{2B}, \tag{2.6}$$

and the second is known as the longitudinal adiabatic invariant

$$\mathcal{J} = \oint (mv_{\parallel} + qA_{\parallel})\,\mathrm{d}s, \tag{2.7}$$

where s is the distance along the magnetic field lines, and $A_{\parallel}$ is the magnetic vector potential, and $v_{\parallel}$ the velocity, in the direction of $\boldsymbol{B}$.

2.2 Kinetic Description

A complete description of a plasma consisting of N charged particles acted on by the Lorentz force $\boldsymbol{F}_{\mathrm{L}} = q_{\alpha}(\boldsymbol{E} + \boldsymbol{v} \times \boldsymbol{B})$, where $\boldsymbol{E}$ is the electric field and $\boldsymbol{v}$ is the particle velocity, would require solving a system of $6N+12$ coupled equations. These consist of $6N$ equations of motion (one for each particle and dimension in the 6-dimensional phase-space), the four equations for charge and current densities ϱ, $\boldsymbol{j}$, as well as Maxwell's 8 equations. Given that the number of particles in a plasma is statistically large, this is computationally unfeasible by a large margin.

Taking a statistical approach, one can construct the distribution function $f_{\alpha}(t, \boldsymbol{x}, \boldsymbol{v})$. The exact distribution function is defined as the density of particles of species α at position $\boldsymbol{x}$ and velocity $\boldsymbol{v}$ in phase-space at time t. This is then smoothed over a volume element of phase-space containing many particles, small enough to not contain significant variations of the exact distribution function, to get f_{α}. It is then possible to calculate the evolution of f_{α} for ions and electrons instead of the motion of individual particles. This is the kinetic description of plasmas, which is still a computationally expensive approach, but at least feasible for a wide range of problems.

The governing equation of f_{α} is the Vlasov equation[1]

$$\frac{\partial f_{\alpha}}{\partial t} + \boldsymbol{v} \cdot \nabla f_{\alpha} + \frac{q_{\alpha}}{m_{\alpha}}(\boldsymbol{E} + \boldsymbol{v} \times \boldsymbol{B}) \cdot \nabla_{\boldsymbol{v}} f_{\alpha} = \left(\frac{\partial f_{\alpha}}{\partial t}\right)_{\mathrm{c}}, \tag{2.8}$$

where $\boldsymbol{E}$ and $\boldsymbol{B}$ have been smoothed similarly to f_{α}, and $\nabla_{\boldsymbol{v}}$ denotes the gradient with respect to velocity. The term on the right-hand side is called the collision operator and describes the collective effect of two-particle correlations. A collisionless plasma is one where the left-hand side terms of equation (2.8) dominate and the collision operator can be neglected on the spatio-temporal scales considered. Essentially, if the collisional mean free path of the particles is significantly larger than the system or phenomena of interest, the plasma is collisionless. Many plasma environments in the universe and in the laboratory are collisionless, and these are the types of systems that this thesis will be concerned with.

2.3 Fluid Description

Many physical quantities that describe a plasma are obtained by taking so called velocity moments of the distribution function. These fluid quantities can then be

---

[1] Often called the Boltzmann equation when including the collision operator.

used to describe plasma evolution through a set of fluid equations for each particle species, obtained by taking different velocity moments of the Vlasov equation. This plasma model, the fluid description, removes the velocity degrees of freedom from the equations, which represents a dramatic reduction of the computational cost as compared to the kinetic description. Important to note is that the fluid model does not require any assumptions about the distribution function, which allows for anisotropy in quantities like the pressure to be present due to an anisotropic distribution function in velocity space.

2.3.1 Velocity Moments and Fluid Quantities

The distribution function is a phase-space density, which means that integrating $f_\alpha(t,\boldsymbol{x},\boldsymbol{v})$ over velocity-space gives the number density in regular space $n_\alpha(t,\boldsymbol{x})$ for that species. Multiplying $f_\alpha(t,\boldsymbol{x},\boldsymbol{v})$ by $\boldsymbol{v}$ and integrating over velocity space gives $n_\alpha(t,\boldsymbol{x})\boldsymbol{u}_\alpha(t,\boldsymbol{x})$, where $\boldsymbol{u}_\alpha$ is the mean, or fluid, velocity. In a similar manner, it is possible to construct other useful velocity-space averaged quantities by multiplying f_α with some power of $\boldsymbol{v}$ or $(\boldsymbol{v}-\boldsymbol{u}_\alpha)$ and integrating over velocity-space. This procedure is known as taking velocity moments of f_α. The order of the moment refers to the power of the velocity that is used, so that for example n_α is the zeroth order velocity moment of f_α. Some important fluid quantities defined in this way are given by

$$n_\alpha(t,\boldsymbol{x}) = \int f_\alpha \,\mathrm{d}^3v \qquad \text{Number density} \tag{2.9}$$

$$\boldsymbol{u}_\alpha(t,\boldsymbol{x}) = \frac{1}{n_\alpha}\int \boldsymbol{v} f_\alpha \,\mathrm{d}^3v \qquad \text{Fluid velocity} \tag{2.10}$$

$$\boldsymbol{p}_\alpha(t,\boldsymbol{x}) = m_\alpha \int (\boldsymbol{v}-\boldsymbol{u}_\alpha)(\boldsymbol{v}-\boldsymbol{u}_\alpha) f_\alpha \,\mathrm{d}^3v \qquad \text{Pressure tensor} \tag{2.11}$$

$$\boldsymbol{q}_\alpha(t,\boldsymbol{x}) = m_\alpha \int (\boldsymbol{v}-\boldsymbol{u}_\alpha)(\boldsymbol{v}-\boldsymbol{u}_\alpha)(\boldsymbol{v}-\boldsymbol{u}_\alpha) f_\alpha \,\mathrm{d}^3v \qquad \text{Heat flux tensor.} \tag{2.12}$$

Instead of the pressure and heat flux tensors defined in equations (2.11) and (2.12), it is possible to work with $\boldsymbol{P}_\alpha(t,\boldsymbol{x}) = m_\alpha \int \boldsymbol{v}\boldsymbol{v} f_\alpha \,\mathrm{d}^3v$ and $\boldsymbol{Q}_\alpha(t,\boldsymbol{x}) = m_\alpha \int \boldsymbol{v}\boldsymbol{v}\boldsymbol{v} f_\alpha \,\mathrm{d}^3v$, known as the stress and energy flux tensors.

From the pressure tensor, defined in equation (2.11), the scalar pressure and temperature are defined as

$$p_\alpha(t,\boldsymbol{x}) = \frac{1}{3}\,\mathrm{Tr}[\boldsymbol{p}_\alpha] \tag{2.13}$$

$$T_\alpha(t,\boldsymbol{x}) = \frac{p_\alpha}{n_\alpha}. \tag{2.14}$$

This definition is chosen consistently with the fact that a fully isotropic pressure tensor, as that which is obtained when the plasma is in thermodynamic equilibrium and the distribution function is Maxwellian, is diagonal with all diagonal elements equal to the same scalar pressure.

Sometimes it is of interest to study pressure anisotropy in a plasma, for instance because it may drive instabilities, or lead to other observable features. Anisotropy refers to the fact that the pressure need not be equal in all spatial directions. In the magnetized regime, pressure anisotropy measures use the local magnetic field lines as a reference direction, where $p_{\parallel,\alpha}$ is the pressure in the direction of $\boldsymbol{B}$ and $p_{\perp,\alpha}$ is the pressure perpendicular to $\boldsymbol{B}$. The pressure anisotropy is commonly defined as $\mathit{\Delta}_\alpha = p_{\perp,\alpha}/p_{\parallel,\alpha} - 1$ [5]. However, this is only valid for magnetized plasmas, and some other definition of $\mathit{\Delta}_\alpha$ needs to be used in the non-magnetized regime. One possibility is to use the eigenvector of $\boldsymbol{\mathsf{p}}_\alpha$ with the largest eigenvalue $p_{\alpha,\mathrm{max}}$ as the reference direction. Taking $p_{\alpha,\mathrm{min}}$ to be the average of the other two eigenvalues, the pressure anisotropy can be defined as

$$\mathit{\Delta}_\alpha = \frac{p_{\alpha,\mathrm{max}}}{p_{\alpha,\mathrm{min}}} - 1 \tag{2.15}$$

for non-magnetized plasmas [7]. Additionally, it can be noted that in a strongly magnetized plasma, the off-diagonal elements of the pressure tensor (in a coordinate system locally aligned with $\boldsymbol{B}$) are very small, while in a non-magnetized plasma off-diagonal pressure tensor elements can also be dynamically significant.

2.3.2 The 10-Moment Equations

In the fluid description of plasmas, velocity moments of increasing order are taken of the Vlasov equation (2.8) to get a system of partial differential equations containing only velocity-space averaged quantities. Taking the zeroth, first and second order velocity moments of the collisionless Vlasov equation and rearranging terms results in the following equations:

$$\frac{\partial n}{\partial t} + \frac{\partial}{\partial x_j}(n u_j) = 0 \tag{2.16}$$

$$mn\frac{\partial u_j}{\partial t} + mnu_k\frac{\partial u_j}{\partial x_k} + \frac{\partial \mathsf{p}_{jk}}{\partial x_k} = nq\Big[E_j + \epsilon_{jkl}u_k B_l\Big] \tag{2.17}$$

$$\frac{\partial \mathsf{p}_{jk}}{\partial t} + \frac{\partial}{\partial x_l}(\mathsf{p}_{jk}u_l) + \mathsf{p}_{jl}\frac{\partial u_k}{\partial x_l} + \mathsf{p}_{kl}\frac{\partial u_j}{\partial x_l} + \frac{\partial q_{jkl}}{\partial x_l} = \frac{q}{m}\Big[\epsilon_{jlm}\mathsf{p}_{lk}B_m + \epsilon_{klm}\mathsf{p}_{lj}B_m\Big]. \tag{2.18}$$

Here ϵ is the Levi-Civita tensor, the species index α is omitted, and index notation refers to vector and tensor components (sums over repeated component indices is implied).

Noteworthy here is that the equation describing the evolution of a certain velocity moment of f — n, $\boldsymbol{u}$ or $\boldsymbol{\mathsf{p}}$ — always includes a one order higher velocity moment of f — $\boldsymbol{u}$, $\boldsymbol{\mathsf{p}}$ or $\boldsymbol{q}$. The evolution of this higher order quantity is in turn determined by the next order moment equation. Therefore taking velocity moments of the Vlasov equation results in a hierarchy of fluid equations that needs to be closed at some order, neglecting higher-order contributions. Usually this is done by prescribing a *closure* for the heat flux tensor in equation (2.18) in terms of the lower order moments of f (n, $\boldsymbol{u}$, $\boldsymbol{\mathsf{p}}$), which closes the equation system (2.16)–(2.18). Equations (2.16), (2.17) and (2.18) are called the continuity, momentum and energy equations respectively. When prescribing a closure for $\boldsymbol{q}$ in terms of n, $\boldsymbol{u}$ and $\boldsymbol{\mathsf{p}}$, equations (2.16)–(2.18) are known together as the 10-moment equations, since the system for each particle species describes the evolution of the 10 lowest-order independent moments of f: n, $\boldsymbol{u}$ (3 components) and $\boldsymbol{p}$ (symmetric — 6 independent components).

In strongly collisional systems accurate fluid closures can be theoretically obtained, because collisions render the physics local and keeps the system close to thermodynamic equilibrium. In collisionless systems however, it is much more difficult to find closures — they can be ad-hoc or chosen to fit a specific physics scenario [13]. The drawback of physically motivated collisionless closures is often that they require certain assumptions to be made, such as exact adiabaticity, which are not valid in most relevant physics problems for collisionless systems. Recently, a more systematic search for collisionless closures has begun. Sparse regression has for example been used to find relevant closure terms by comparing the results of collisionless fluid and kinetic simulations [13]. In this thesis ad-hoc closures, each with a free parameter, will be used.

2.4 Magnetohydrodynamics

A further simplified plasma description can be obtained by considering the plasma as a single conductive fluid, by combining the fluid moment equations for electrons and ions. This is known as magnetohydrodynamics, or MHD. The total mass density, the (MHD) flow velocity and the MHD pressure tensor are defined as

$$\rho_{\mathrm{m}} = \sum_{\alpha=e,i} m_\alpha n_\alpha \tag{2.19}$$

$$\boldsymbol{U} = \frac{1}{\rho_{\mathrm{m}}} \sum_{\alpha=e,i} m_\alpha n_\alpha \boldsymbol{u}_\alpha \tag{2.20}$$

$$\boldsymbol{p}^* = \sum_{\alpha=e,i} m_\alpha \int (\boldsymbol{v}-\boldsymbol{U})(\boldsymbol{v}-\boldsymbol{U}) f_\alpha \, \mathrm{d}^3 v. \tag{2.21}$$

Multiplying equation (2.16) for electrons and ions with the particle mass of the species and summing the equations gives the MHD continuity equation (2.22). Summing the momentum equations for electrons and ions, using $\varrho \approx 0$ since the plasma is quasineutral, gives the MHD momentum equation (2.23). When including the effect of collisions, it is also possible to derive an approximate MHD Ohm's law that applies for sufficiently magnetized plasmas, given in equation (2.24):

$$\frac{\partial \rho_{\mathrm{m}}}{\partial t} + \nabla \cdot (\rho_{\mathrm{m}} \boldsymbol{U}) = 0 \tag{2.22}$$

$$\rho_{\mathrm{m}} \frac{\partial \boldsymbol{U}}{\partial t} + \rho_{\mathrm{m}} (\boldsymbol{U} \cdot \nabla) \boldsymbol{U} + \nabla \cdot \boldsymbol{p}^* = \boldsymbol{j} \times \boldsymbol{B} \tag{2.23}$$

$$\boldsymbol{E} + \boldsymbol{U} \times \boldsymbol{B} = \eta \boldsymbol{j}. \tag{2.24}$$

This specific form of the MHD Ohm's law is obtained by considering the difference between the ion and electron momentum equations multiplied by the other species' respective particle mass [11]. Here η is the resistivity. The situation where the right-hand side term is negligible in Ohm's law, essentially when $\eta \approx 0$, is known as ideal MHD, while the formalism using the current form is referred to as resistive MHD. Other MHD formulations also exist, which will not be treated here, that have additional terms on the right-hand side.

An important concept in ideal MHD is flux-freezing. It is possible to show that for a plasma described by ideal MHD, the magnetic flux, $\mathit{\Phi}$, through the closed contour of a surface moving with the local flow velocity $\boldsymbol{U}$ is constant:

$$\frac{\mathrm{d}\mathit{\Phi}}{\mathrm{d}t} = 0. \tag{2.25}$$

Here, the convective derivative, describing the change with time as seen by a coordinate system moving with velocity $\boldsymbol{U}$, is defined as

$$\frac{\mathrm{d}}{\mathrm{d}t} = \frac{\partial}{\partial t} + \boldsymbol{U} \cdot \nabla. \tag{2.26}$$

Consequently, magnetic field lines are “frozen” into the plasma flow in ideal MHD. A flow that for example stretches the plasma also pushes magnetic field lines closer together, increasing the field strength B. It can be noted that the frozen-in condition is quite accurately satisfied in collisionless space and astrophysical plasmas even though MHD is not strictly speaking applicable to them. However, it is not exactly satisfied, which is essential for dynamo action to be possible [14] — this will be discussed further in chapter 3.

Usually in an MHD treatment of plasma, a prescribed closure, or equation of state, is provided for the pressure tensor $\boldsymbol{p}^*$ rather than the heat flux tensor. This means that the two relevant fluid equations are (2.22) and (2.23). The pressure is usually taken to be diagonal and either isotropic with scalar pressure p^*, or having the pressure $p_\parallel^*$ in the magnetic field direction and $p_\perp^*$ in the other directions. The latter is known as the Chew-Goldberger-Low (CGL) model [15], and the difference between the two cases in a coordinate system where the z-axis is aligned with the local magnetic field direction can be seen in the form of $\boldsymbol{p}^*$:

$$\boldsymbol{p}^* = \begin{bmatrix} p^* & 0 & 0 \\ 0 & p^* & 0 \\ 0 & 0 & p^* \end{bmatrix} = p^* \boldsymbol{I} \qquad \text{Isotropic} \tag{2.27}$$

$$\boldsymbol{p}^* = \begin{bmatrix} p_\perp^* & 0 & 0 \\ 0 & p_\perp^* & 0 \\ 0 & 0 & p_\parallel^* \end{bmatrix} = p_\perp^* \boldsymbol{I} + (p_\parallel^* - p_\perp^*)\boldsymbol{bb} \qquad \text{CGL.} \tag{2.28}$$

Here $\boldsymbol{I}$ is the two-dimensional identity tensor, $\boldsymbol{b} = \boldsymbol{B}/B$ is the unit vector in the magnetic field direction and the expressions on the right hand side are valid in general coordinate systems.

Any anisotropy that develops in the pressure would be equilibrated by collisions, provided that these are frequent in the plasma. Therefore the CGL case allowing for persisting different $p_\perp^*$ and $p_\parallel^*$ is essentially the closest to a collisionless model for $\boldsymbol{p}^*$. If the plasma is completely magnetized and thus exactly conserves the adiabatic invariants in equations (2.6) and (2.7), it can be shown that the parallel and perpendicular pressures must obey the CGL equations

$$\frac{\mathrm{d}}{\mathrm{d}t}\left(\frac{p_{\perp}^{*}}{\rho_{\mathrm{m}}B}\right) = 0 \tag{2.29}$$

$$\frac{\mathrm{d}}{\mathrm{d}t}\left(\frac{p_{\parallel}^{*}B^{2}}{\rho_{\mathrm{m}}^{3}}\right) = 0, \tag{2.30}$$

when neglecting heat flux terms and collisions [15]. The CGL model is one of the simplest collisionless closures. It turns out that the CGL equations are the statistical equivalents of the first two adiabatic invariants, with equation (2.29) corresponding to μ-conservation and equation (2.30) corresponding to $\mathcal{J}$-conservation [1].

3

Dynamo Theory

The dynamo process, where tiny seed magnetic fields can be exponentially amplified and sustained in turbulent plasmas, is believed to be the mechanism behind the formation of observed astrophysical magnetic fields [1]. Dynamo theory aims to describe and answer questions about this phenomenon, like in what physical regimes they are possible and how fast the amplification of the magnetic field is, in order to better understand the origin of cosmic magnetization.

This chapter introduces the traditional MHD description of the dynamo problem, discusses the conditions under which a dynamo is possible, and furthermore the possibility of treating dynamos with more advanced fluid descriptions for collisionless plasmas, where the classical description is not valid. Unless otherwise stated, the information in this chapter is based on [1].

3.1 Classical Dynamo Theory

The classical treatment of dynamos relies on the MHD formalism, where the relevant equations are (2.22)–(2.24) combined with Maxwell's equations. The induction equation

$$\frac{\partial \boldsymbol{B}}{\partial t} = \nabla \times (\boldsymbol{U} \times \boldsymbol{B}) + \eta_{\mathrm{m}} \mathit{\Delta} \boldsymbol{B} \tag{3.1}$$

is obtained by combining Maxwell's equations with the MHD Ohm's law, equation (2.24), and defining the magnetic diffusivity $\eta_{\mathrm{m}} = \eta/\mu_0$, where μ_0 is the vacuum permeability. Notably, in the $\boldsymbol{U} \approx 0$ limit, this corresponds to magnetic diffusion. A spatially sinusoidal magnetic field will decay exponentially with time in this case. If $\boldsymbol{U}$ is non-zero, but its dependence on $\boldsymbol{B}$ is negligible — which is the case in MHD when $\boldsymbol{B}$ is very small — equation (3.1) is a linear equation in $\boldsymbol{B}$. In that case it can have eigenfunctions potentially corresponding to exponentially growing or decaying solutions. The so called kinematic phase of the dynamo process, of exponential magnetic field growth from small seed fields, can therefore be treated as an eigenvalue problem in the limit where the flow is independent of $\boldsymbol{B}$.

A slightly modified version of the momentum equation (2.23) is usually used in dynamo theory:

$$\rho_{\mathrm{m}} \frac{\partial \boldsymbol{U}}{\partial t} + \rho_{\mathrm{m}} (\boldsymbol{U} \cdot \nabla) \boldsymbol{U} = -\nabla p^* + \boldsymbol{f}_{\mathrm{visc}} + \boldsymbol{j} \times \boldsymbol{B} + \boldsymbol{f}(t, \boldsymbol{x}), \tag{3.2}$$

where $\boldsymbol{f}$ is a force density expressing the effect of large-scale mechanisms driving the flow [2]. The pressure tensor term has been separated into the scalar pressure gradient and the divergence of the remaining traceless pressure tensor, which is assumed to represent a viscous force density term $\boldsymbol{f}_{\text{visc}}$, that is typically small. The viscous term being small allows the development of a turbulent inertial range in physically interesting systems. However, it is worth considering the role of the viscous term on the dynamics in systems where the turbulent flow drive is negligible. In the incompressible limit, when ρ_{m} is approximately constant and $\nabla \cdot \boldsymbol{U} \approx 0$, the viscous force density is taken to be $\boldsymbol{f}_{\text{visc}} = \nu \rho_{\text{m}} \mathit{\Delta} \boldsymbol{U}$, where ν is the kinematic viscosity [2]. Equation (3.2) then describes viscous diffusion of the flow in the absence of external forcing, given that the time derivative and viscosity terms dominate. This would occur when the magnetic field, pressure gradient and non-linear effects are small. Like for the magnetic field in equation (3.1), diffusion of a spatially sinusoidal flow in equation (3.2) would lead to an exponential decay of the flow velocity.

Dynamo growth is a growth of the magnetic energy in the system. It can be shown that, when the net Poynting flux through the system boundary is 0, any growth of magnetic energy comes from a reduction in kinetic energy. This can be directly observed from the evolution equation for the total magnetic energy

$$\frac{\mathrm{d}}{\mathrm{d}t} \int_V E_B \, \mathrm{d}V = -\int_V \boldsymbol{U} \cdot (\boldsymbol{j} \times \boldsymbol{B}) \, \mathrm{d}V - \int_V \eta j^2 \, \mathrm{d}V - \oint_{\partial V} \frac{\boldsymbol{E} \times \boldsymbol{B}}{\mu_0} \cdot \mathrm{d}\boldsymbol{S}, \tag{3.3}$$

where $E_B = B^2/(2\mu_0)$ is the magnetic energy density [2]. The second term on the right-hand side corresponds to resistive energy losses through Ohmic heating and the last term to the Poynting flux through the volume surface. Any increase in the magnetic energy must therefore come from the first term, by the Lorentz force doing work against the flow, which in turn decreases the kinetic energy in the flows. A large-scale driven flow can therefore feed the magnetic energy. Studying equation (3.1) closer in the incompressible limit, it is seen that $\nabla \times (\boldsymbol{U} \times \boldsymbol{B}) = (\boldsymbol{B} \cdot \nabla)\boldsymbol{U} - (\boldsymbol{U} \cdot \nabla)\boldsymbol{B}$. The first term represents a stretching, while the second term corresponds to an advection, of the magnetic field lines. In an incompressible plasma it can therefore be discerned that magnetic stretching by a sheared flow (roughly defined as a flow where the flow speed varies significantly perpendicular to the flow velocity) is needed for magnetic field growth.

However, not all types of flows can generate dynamos, and not all magnetic field geometries can be obtained by dynamos. There are a number of “anti-dynamo theorems” which state the impossibility for the dynamo mechanism to cause magnetic field growth in certain constrained geometries. Two examples are Cowling’s theorem [16] — dynamo action does not permit the growth of an axisymmetric magnetic field — and Zel’dovich’s theorem [17, 18] — purely two-dimensional flows do not allow for magnetic field growth from dynamos. Because many types of limitations in geometry similar to these can render magnetic field growth by the dynamo mechanism impossible, the dynamo problem is essentially three-dimensional in nature. A dynamo can only be excited by a sufficiently geometrically complex flow.

It is important to note that random three-dimensional sheared flows allow for dynamos to grow, which is why this mechanism can generate magnetic fields in nature, even in systems without large-scale order. There is however a practical use of analytical flows when modeling dynamos, since these can excite dynamos more efficiently, and the corresponding growth rates can be obtained [19]. An example of an analytical flow that has complicated enough geometry to allow for dynamo growth is the Galloway-Proctor (GP) flow [20], which has three non-zero components that depend on two spatial dimensions and time:

$$\boldsymbol{U}_{\mathrm{GP}}(t, \boldsymbol{x}) = u_0 \begin{bmatrix} A\sin(k_0 z + \sin(\omega t)) + C\cos(k_0 y + \cos(\omega t)) \\ A\cos(k_0 z + \sin(\omega t)) \\ C\sin(k_0 y + \cos(\omega t)) \end{bmatrix}, \tag{3.4}$$

where ω is the angular frequency of time oscillations, $k_0 = 2\pi/L_0$, and u_0 and L_0 are a characteristic speed and length scale of the flow. Given appropriately chosen constants A and C, this flow is chaotic. This has a relevance in that a chaotic flow can drive so called fast dynamos — ones that are active even in the presence of extremely low resistivity, to be discussed section 3.1.2.

3.1.1 Reynolds Numbers

In classical resistive MHD, it is possible to define dimensionless quantities describing the relative characteristic sizes of different terms in equations (3.1) and (3.2). These can then be used to characterize dynamos, as well as define regions in parameter space where dynamo action is possible within the classical MHD description.

Comparing the characteristic size of the curl-term and the diffusive term in equation (3.1), representing mixing/stretching and resistivity, respectively, gives the magnetic Reynolds number

$$Rm = \frac{u_0 L_0}{\eta_{\mathrm{m}}}. \tag{3.5}$$

Here L_0 and u_0 are the typical length scale and velocity fluctuation size at the largest scale of the flow, where energy is typically injected into the system. Doing the same sort of comparison in equation (3.2) for the advection term and the diffusive term, representing inertia and viscosity, results in the kinematic, or fluid, Reynolds number

$$Re = \frac{u_0 L_0}{\nu}. \tag{3.6}$$

When these dimensionless numbers are large, which they are in astrophysically relevant scenarios, the viscous damping of flows and the resistive damping of magnetic fields, respectively, are tiny on the scale of the system size L_0. For the fluid Reynolds number this allows turbulent cascades to develop, where the energy in flows moves towards smaller and smaller spatial scales. The flow eventually develops large enough gradients that viscosity can dissipate the energy irreversibly at very fine scales. Considering the magnetic field, that in the high-Rm limit is essentially frozen into, and advects along with, the flow on large scales, the turbulence also results in the magnetic field reaching tiny scales before the small resistivity is sufficient to dissipate it.

3.1.2 Fast Dynamos

In order for a magnetic field to irreversibly grow in an MHD dynamo, a finite magnetic diffusion is necessary, which means that the magnetic Reynolds number, even if large, needs to be finite. Some dynamos have magnetic field growth rates that decay with increasing Rm (slow dynamos). They are not suitable to explain magnetic field growth observed in astrophysical systems where Rm is enormous. Other dynamos, which have chaotic flows, have a growth rate that increases with, and asymptotically becomes independent of, Rm for large values of Rm. These “fast dynamos” are then astrophysically relevant. The GP-flow introduced in equation (3.4) is thought to produce fast dynamos.

The cartoon picture of how the fast dynamo operates to amplify magnetic fields exponentially is summarized in the “stretch-twist-fold-merge mechanism”, illustrated in figure 3.1. To understand it, a closed magnetic field loop with, for example, a clockwise directionality of the field lines contained in the loop can be considered. A sheared flow can stretch the loop in one direction of its spatial plane, because the field is more or less frozen into the flow as discussed in section 2.4. This results in a multiplicative amplification of the field strength as the distance between the field lines in the loop decreases with the stretching. If one end of the stretched loop is twisted 180 degrees, and subsequently folded over the mid-point where the loop crosses over itself, a double loop has been made. All field lines in the double loop once again have clockwise directionality in the plane. At this point a finite, but possibly tiny, magnetic diffusivity is necessary for the two loops to merge into one. The original configuration is then retained, with a multiplicative amplification of the initial field strength. A repetition of this mechanism clearly leads to exponential growth of the field strength on timescales characteristic to the sheared flow.

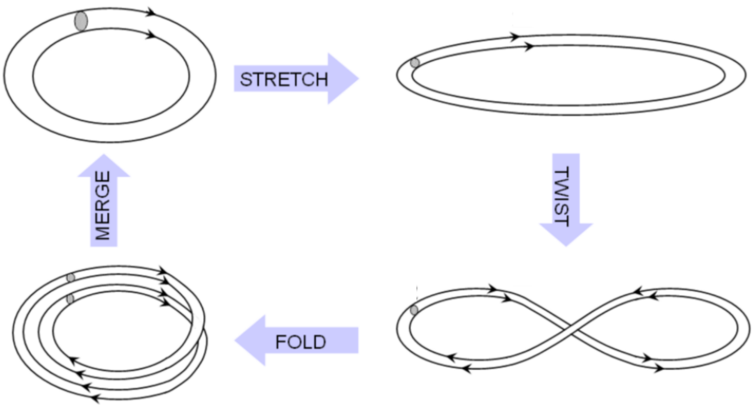

Figure 3.1: The “stretch-twist-fold-merge mechanism” of the fast dynamo. [Figure adopted and modified from: www.mpifr-bonn.mpg.de/3622111/lectures6-9.pdf.]

3.2 Collisionless Dynamos

Space and astrophysical systems of interest in dynamo research, apart from the interior of stars and planets, are essentially collisionless. In these systems the effect of small-scale (kinetic) processes like plasma instabilities, which can for example be generated by pressure anisotropy, typically dominate over collisional effects. Because the classical MHD treatment of dynamos assumes that collisions dominate over other small-scale processes, does not evolve the full pressure tensor, and discards higher-order moments like the heat flux, it is inherently not valid for these types of weakly collisional systems — at least not without employing some collisionless closure, like the CGL-closure, which gives rise to other problems for dynamos to be discussed in section 3.3. Despite the fact that this has been understood, the MHD treatment of dynamos as presented in section 3.1 is still the most commonly used method to model dynamos. This is simply because modeling collisionless dynamos with more advanced models is extremely difficult and numerically costly, due to their 3D and multi-scale nature. If a kinetic description of collisionless dynamos is to be used, it poses such a high numerical demand that it seriously limits the possibilities of what can be modeled. This is why so far, only hybrid modeling (with kinetic ions and isothermal massless fluid electrons) [3, 4] and so called pair-plasmas (i.e. electron-positron plasmas, with unit mass-ratio between the species) [5], have been used to treat the collisionless dynamo problem (semi-) kinetically.

The computational challenge motivates the use of simplified models, that can still retain some kinetic physics — fluid models. For these models, closures of the fluid equations can be used to describe the effects of small-scale phenomena in collisionless plasmas for both electrons and ions.

Much of the dynamo research done so far has characterized dynamos based on dimensionless MHD quantities like the fluid and magnetic Reynolds numbers, defined in equations (3.6) and (3.5). These are, however, not well defined in a collisionless system, that does not have explicit values of the kinematic viscosity or magnetic diffusivity. It is therefore useful to construct analogous quantities, effective fluid and magnetic Reynolds numbers, for a fluid description of collisionless plasmas. The Reynolds numbers essentially compare the typical rates at which magnetic fields and flows respectively are generated and damped on the system scale in resistive MHD, which can be rewritten and interpreted according to

$$Rm = \frac{u_0 L_0}{\eta_\mathrm{m}} = \frac{u_0/L_0}{\eta_\mathrm{m}/L_0^2} \sim \left.\frac{\text{growth rate from field line stretching}}{\text{magnetic diffusion rate}}\right|_{\text{system scale}} \tag{3.7}$$

$$Re = \frac{u_0 L_0}{\nu} = \frac{u_0/L_0}{\nu/L_0^2} \sim \left.\frac{\text{growth rate from inertial processes}}{\text{viscous flow damping rate}}\right|_{\text{system scale}} . \tag{3.8}$$

To replace the typical damping rates, defined using ν and η_m in resistive (collisional) MHD, to obtain effective Reynolds numbers for a collisionless model, one can study the effect of varying free parameters of the fluid closure employed in the model on the magnetic field and flow damping rates in non-driven simulations. The generalized, effective Reynolds numbers can be written

$$Rm = \frac{u_0/L_0}{\gamma_B} \tag{3.9}$$

$$Re = \frac{u_0/L_0}{\gamma_U} \tag{3.10}$$

where γ_B and γ_U are the magnetic field and flow damping rates respectively of the collisionless system. An analysis of this type will be conducted in chapter 4 for the collisional fluid model used in this thesis. This will characterize how the effective Reynolds numbers depend on the closure, which is supposed to describe the effect of the small-scale processes that dominate in collisionless systems, that can cause damping of flows and magnetic fields similarly to collisions.

3.3 Magnetic Moment Conservation in the CGL-Model

In the same manner as described for MHD in section 2.4, the CGL-model can also be used as a simple collisionless closure in the fluid plasma description. The pressure tensors for electrons and ions must then obey their respective CGL equations, analogous to equations (2.29) and (2.30) with $p_\perp^* \to p_{\perp,\alpha}$, $p_\parallel^* \to p_{\parallel,\alpha}$ and $\rho_\mathrm{m} \to n_\alpha$. As stated previously the CGL equation for the perpendicular pressure represents magnetic moment conservation for magnetized plasmas. This would imply that growth of the magnetic energy, which grows with B, is accompanied by growth of the perpendicular kinetic energy of the plasma particles. However, it has been shown in simulations with enforced CGL-equations for MHD [14] that this counterintuitive perpendicular heating does not occur, and thus that the magnetic energy can not grow substantially. Therefore it can be stated that another "anti-dynamo theorem" is that dynamos are impossible in the adiabatic, or CGL, limit, where the magnetic moment is exactly conserved [14]. This turns out to be true even if only one particle species, the electrons or the ions, obeys magnetic moment conservation [14].

Magnetic moment conservation is broken by collisions, and the anti-dynamo theorem concerning this is therefore not an obstacle for the dynamo mechanism in collisional plasmas. Other kinetic-scale processes, like finite-Larmor-radius effects in the unmagnetized regime and kinetic instabilities in the magnetized regime, can also break μ-conservation. Dynamos in collisionless plasmas are therefore not impossible, but rather rely on processes that are not captured by the simple CGL-closure, and similar closures preserving the adiabatic invariants. It turns out that when combining the two CGL equations for either electrons or ions, the following equation can be obtained:

$$\frac{\mathrm{d}}{\mathrm{d}t}(p_{\perp,\alpha} - p_{\parallel,\alpha}) = (p_{\perp,\alpha} + 2p_{\parallel,\alpha})\frac{\mathrm{d}\ln B}{\mathrm{d}t} + (p_{\perp,\alpha} - 3p_{\parallel,\alpha})\frac{\mathrm{d}\ln n_\alpha}{\mathrm{d}t}. \tag{3.11}$$

Any increase of the magnetic field is seen to correspond to an increasing pressure anisotropy on the left-hand side. There are many kinetic, pressure anisotropy-driven plasma instabilities that could be activated by this, break μ-conservation and relax the pressure anisotropy, allowing the magnetic field to grow through dynamo action. Two notable candidates are the ion firehose and mirror instabilities [21].

3.4 The Seed Problem

While the dynamo process explains how extremely small magnetic fields can be exponentially amplified to the levels present in astrophysical systems, it does not answer the question of what mechanism the tiny "seed" fields required for dynamos originate from. One possibility is that primordial seed fields were generated in the early universe [22–24]. These primordial fields would be too small to make up the cosmic magnetization observed today, and it is not certain if they could be sustained for long enough to participate in the dynamo process [25]. An astrophysical possibility for seed generation that can occur in a wide variety of contexts [26–31] is the mechanism known as the "Biermann battery" [32], where weak, but relatively large-scale, magnetic fields can arise from charge separation in an astrophysical plasma [25].

An alternative astrophysical seed generation mechanism is the Weibel instability, that can produce magnetic fields in counter-streaming plasma scenarios [33], or more naturally, in the presence of sheared flows [7]. The Weibel instability is somewhat unique among the possible seed generation mechanisms in that it saturates when the plasma starts to become magnetized, at much higher magnetic field levels than the others [7]. Compared to other seed mechanisms like the Biermann battery, however, the seeds produced by the Weibel instability have very small spatial scales [25]. It is particularly interesting as a seed generation mechanism in astrophysical contexts since it only requires pressure anisotropy in an unmagnetized, collisionless plasma to generate large seed fields [7]. The Weibel instability has often been overlooked in the problem of cosmic seed generation in large-scale turbulent systems like those relevant for dynamos [7], because it usually requires kinetic modeling. However, it could be present when using fluid models evolving the full pressure tensor.

In chapter 5, where dynamo simulations will be performed using a fluid model evolving the full pressure tensors of both electrons and ions, it will turn out that a pressure anisotropy-driven instability is active in certain cases, and generates a relatively large seed magnetic field. The results will be compared to the magnetic field evolution that is expected of the Weibel instability to study whether this could be the cause. Generalizing the analytical estimates of the magnetic field growth rate and most unstable mode given in [7] for the electron Weibel instability in the "linear phase" to apply for either ions or electrons, these are:

$$\gamma_{\mathrm{w},\alpha} \sim \mathit{\Delta}_\alpha^{3/2} \frac{v_{\mathrm{th},\alpha}}{\delta_\alpha} \tag{3.12}$$

$$k_{\mathrm{w},\alpha} \simeq \mathit{\Delta}_\alpha^{1/2} / \delta_\alpha . \tag{3.13}$$

Here $\mathit{\Delta}_\alpha$ is the non-magnetized pressure anisotropy measure defined in equation (2.15), $\gamma_{\mathrm{w},\alpha}$ is the magnetic field growth rate due to the electron or ion Weibel instability and $k_{\mathrm{w},\alpha}$ is the most unstable Weibel mode for each species. The thermal speed here uses the $v_{\mathrm{th},\alpha} = \sqrt{T_\alpha / n_\alpha}$ convention, differing by a factor of $\sqrt{2}$ from the conventions used in the rest of this thesis (see equation (2.5)).

3.5 Advanced Fluid Models

From the information presented in the above sections, it is firstly clear that classical MHD dynamo theory is not suitable for modeling collisionless plasma systems, where significant deviations from an isotropic pressure naturally develop. Adding one level of complexity, namely using a collisionless closure like the CGL-model for MHD that allows pressure anisotropy to develop, builds magnetic moment conservation into the description. This is still insufficient to model dynamos, due to μ-conservation of even one species corresponding to an anti-dynamo theorem. Treating the electrons simplistically since they are more collisional than the ions, as done in hybrid simulations, is therefore not entirely motivated either. It has also been found in collisionless plasmas that even off-diagonal pressure tensor terms are important in balancing induced electric fields in the absence of collisional resistivity [34].

These arguments, together with the aim of retaining the Weibel instability, which is an important seed field generation candidate, imply the need for a model where the entire pressure tensor is evolved for both species. This corresponds to a 10-moment fluid model, based on equations (2.16), (2.17) and (2.18), where the closure is employed at the heat flux level.

3.5.1 Gkeyll's 10-Moment Collisionless Fluid Solver

One of the few currently available 10-moment collisionless fluid solvers, that evolves the full pressure tensors of both electrons and ions, is the `Gkeyll` ten-moment multifluid code [8]. This is the solver used in this thesis, and the code framework is publicly available at [10]. It solves the collisionless 10-moment equations (2.16), (2.17) and (2.18) coupled to the full Maxwell equations, has been benchmarked to classical test problems [8], used to simulate magnetospheres of moons and planets [35–38], and other physics problems [39–46] including various magnetic reconnection scenarios.

There are two closures currently available for the 10-moment collisionless fluid solver of `Gkeyll`. The isotropization closure drives the system toward an isotropic pressure, and the gradient-based closure essentially defines the heat flux tensor as gradients of the temperature tensor multiplied by a thermal conductivity [45]. The definitions of the closures are:

$$\frac{\partial q_{\alpha,ijk}}{\partial x_k} = k_{0,\alpha} v_{\mathrm{th},\alpha} (p_{\alpha,ij} - p_\alpha \delta_{ij}) \qquad \text{Isotropization closure} \tag{3.14}$$

$$q_{\alpha,ijk} = \frac{n_\alpha v_{\mathrm{th},\alpha}}{6\, k_{0,\alpha}} \frac{\partial}{\partial x_{[i}} T_{\alpha,jk]} \qquad \text{Gradient-based closure.} \tag{3.15}$$

Here δ_{ij} is the two-dimensional identity tensor, the temperature tensor is defined as $\mathsf{T}_{\alpha,ij} = \mathsf{p}_{\alpha,ij}/n_\alpha$, and the square brackets indicate a sum over all permutations of the component indices i, j, k (of which there are $3! = 6$, so that the factor $1/6$ in the expression results in an average of the permutations). It should be noted that `Gkeyll` uses the convention $v_{\mathrm{th},\alpha} = \sqrt{T_\alpha/m_\alpha}$ in the equations given above, differing by a factor $\sqrt{2}$ from the conventions used throughout the rest of this thesis (see equation (2.5)). The free closure parameters $k_{0,\alpha}$, that can be chosen to take different values for ions and electrons, have the dimension of a wave number and set the overall strength of the closures.

4

Damping of Flows and Magnetic Fields in Collisionless Fluid Simulations

In this chapter, the generalized, effective Reynolds numbers for a collisionless plasma introduced in section 3.2 will be connected to the closure, that represents the effect of kinetic processes dominating in the absence of collisions, by studying the damping of magnetic fields and flows. This is done to get a sense of how the Reynolds numbers, often used to characterize dynamos in the collisional regime, scale with the free parameters of the closure, so that the results of subsequent fluid dynamo simulations can be compared to trends found in MHD dynamo studies.

With the aim of connecting the damping rates of the flow velocity and magnetic field strength, present in the definitions of the effective Reynolds numbers in equations (3.10) and (3.9), to the free closure parameters $k_{0,i}$ and $k_{0,e}$, simple one-dimensional simulations were performed of flow decay and magnetic field decay scenarios. Scans over each of the closure parameters were done in both the flow and magnetic field decay setups. Because of the possible dependence of the decay rates on the flow or magnetic field geometry and characteristic length scales, scans for both decay scenarios were also performed for k_x, corresponding to the wave number of the initial sinusoidally varying flow velocity or magnetic field. For each scan, the decay rate of U or B was calculated in every case in order to establish the dependence of the decay rates on k_x, $k_{0,i}$ and $k_{0,e}$. The decay rates were expected to depend on some power of the scan parameters. Attempts were made to perform these scans for both available fluid closures — the isotropization closure and the gradient-based closure.

As routinely done in computational plasma physics, simulations were performed at a reduced, but still relatively high, mass-ratio of $m_i/m_e = 100$ due to computational constraints, to resolve both ion and electron timescales in the subsequent dynamo simulations that will employ the same mass-ratio. This choice was made because dynamo growth happens on mass flow timescales, that is, ion timescales, while the Weibel instability on develops on timescales given by $\gamma_{\mathrm{w},e}^{-1}$, defined in equation (3.12) using characteristic electron quantities, and the aim is to capture both phenomena in the dynamo simulations.

A weak dependence of the flow damping on $k_{0,e}$, and of the magnetic field damping on $k_{0,i}$, was still expected due to the relatively high mass-ratio used. At a high (more physical) mass-ratio most of the current is carried by the electrons. Thus the magnetic field damping — a result of electron kinetic effects — is expected to be affected by the electron closure, while the damping of the ion flow, that represents most of the MHD (mass) flow, is affected by the ion closure. This separation of electron and ion physics is a feature of all plasmas other than pair-plasmas, and is thus interesting to explore, since simulations similar to the fluid dynamo simulations that will be performed in chapter 5 with the same mass-ratio have only been performed in pair-plasmas previously.

4.1 Normalized Units and Simulation Setup

For simplicity the one-dimensional flow- and magnetic field decay simulations were done using normalized units. In this unit system the constants μ_0, ϵ_0, c, m_e, e and the background electron density n_e are used as a basis of the normalization, and thus all take the value 1 in the normalized unit system. As a consequence of this $\omega_{\mathrm{p},e}$ and δ_e are both 1, so that time is measured in units of $\omega_{\mathrm{p},e}^{-1}$ and length in units of δ_e.

The ions are taken to be singly charged, so that $q_i = -q_e = 1$, and to have the same number density as the electrons $n_i = n_e = 1$. A reduced mass-ratio of $m_i/m_e = 100$, as compared to an electron-proton plasma, is used in order to keep the separation between electron and ion time and length scales limited for computational feasibility. The thermal speed of the electrons, in units of c, is chosen as $v_{\mathrm{th},e} = 0.1$ in order for the bulk of the electron distribution to be non-relativistic. Taking the electron and ion distribution to have the same temperature, the chosen $v_{\mathrm{th},e}$ corresponds to $T_e = T_i = 0.005$ in units of $m_e c^2$. The initial pressure tensors were taken to be isotropic, with scalar pressure $p_\alpha = n_\alpha T_\alpha = 0.005$ for both species. Additional quantities of interest in the normalized units are $v_{\mathrm{th},i} = 0.01$ and $\lambda_{\mathrm{D}} = 0.0707$.

In these one-dimensional simulations, only one spatial direction is resolved, while the full velocity-space is accounted for (e.g. by evolving all components of 3D fluid vectors and tensors, as well as of the fields). The number of cells in the one-dimensional spatial simulation box is chosen as $N_x = 128$ and the spatial resolution as $\mathit{\Delta} x = 0.5$, so that the length of the simulation box is $L_x = N_x \mathit{\Delta} x = 64$. To ensure that the propagation of electromagnetic fields in the plasma, the fastest involved process, is resolved in time, the time step is taken to correspond to the Courant-Friedrichs-Lewy (CFL) condition [47, 48] being exactly fulfilled. The total simulation time t_{max} was adjusted between certain scans, and when needed within a scan, to observe the exponential decay of U or B. Output data was saved for a total number of 91 time points for each case, with the first corresponding to $t = 0$, the last to $t = t_{\mathrm{max}}$ and the rest uniformly distributed during the simulation time. The boundary conditions of the simulation box are taken to be periodic in the x-direction. When not scanning over the closure parameters $k_{0,e}$ and $k_{0,i}$, these were chosen to correspond to a wavelength of $2\mathit{\Delta} x = \delta_e = 1$, so that $k_{0,\alpha} = 2\pi$. Note that $k_{0,e}$ and $k_{0,i}$ have the dimensions of a wave number, but they are just free parameters of the closure. As such, they can take values that correspond to larger or smaller wave numbers than supported by the simulation box size and the spatial resolution.

In the flow decay simulations the electric and magnetic fields were initialized as $\boldsymbol{B} = \boldsymbol{E} = 0$, and ions and electrons were initialized with a common flow velocity in the z-direction, with a size varying sinusoidally in the x-direction:

$$\boldsymbol{u}_{e,i}^{init} = u_{max} \sin(k_x x)\hat{\boldsymbol{z}} = u_{max} \sin\left(N\frac{2\pi x}{L_x}\right)\hat{\boldsymbol{z}}. \tag{4.1}$$

Here $\hat{\boldsymbol{z}}$ is the unit vector in the z-direction, and $k_x = 2\pi N/L_x$ is the wave number corresponding to the wavelength L_x/N, where N is the mode number. The amplitude of the flow is chosen as $u_{max} = 0.2 v_{\mathrm{th},i} = 0.002$, such that the maximal flow velocity is smaller than both the electron and ion thermal speeds and thus remains subsonic, which is relevant for the dynamo simulations that will be presented in chapter 5.

For the simulations of magnetic field decay, the electric field and ion fluid velocity were initialized as $\boldsymbol{E} = \boldsymbol{u}_i^{init} = 0$. The initial magnetic field, and corresponding current density, were chosen consistently, as

$$\begin{aligned} \boldsymbol{B} &= B_{y,0}\cos(k_x x)\hat{\boldsymbol{y}} \\ \boldsymbol{j} &= \frac{1}{\mu_0}\nabla \times \boldsymbol{B} = -B_{y,0}k_x \sin(k_x x)\hat{\boldsymbol{z}}. \end{aligned} \tag{4.2}$$

Letting the electrons carry the entire current initially, an upper limit for the maximum flow speed of the electrons, that can possibly be achieved by the initial magnetic field, was chosen to be $u_{max,e} = 0.01$, such that it is smaller than the electron thermal speed. The maximum allowed current density amplitude is therefore $j_{max} = |q_e n_e u_{max,e}| = 0.01$. Noting that the amplitude of the current density depends on both the magnetic field amplitude and the wave number k_x, an upper limit $k_{x,max}$, corresponding to the mode number $N_{max} = 10$ (so that the geometry is still resolved), was set for k_x in order to fix the value of $B_{y,0}$. Given that $j_{max} = B_{y,0}k_{x,max}$, the value $B_{y,0} = 0.0102$ is obtained and used in the simulations. The maximum magnetic field strength $B_{y,0}$ corresponds to a minimal electron gyroradius of $r_{\mathrm{L},e} = 9.817$, using the assumption $v_{\perp,e} \approx v_{\mathrm{th},e}$. This length scale is clearly resolved in this setup.

4.2 Isotropization Closure

The results of the one-dimensional scans for flow and magnetic field decay using the isotropization closure, corresponding to equation (3.14), are presented in this section.

4.2.1 Flow Decay

To analyze the output from the flow decay simulations the MHD flow velocity was first calculated according to equation (2.20). At each saved time point the values of U^2 were integrated over the simulation box (summed and multiplied by Δx), and the result is simply denoted by U^2 in this section. This quantity is proportional to the kinetic energy density of the flows, $E_U = \rho_\mathrm{m} U^2/2$, integrated over the entire simulation domain. Linear fitting was performed for $\ln(U^2)$ as a function of time t to find the slope, defined as $-2\gamma_U$, where γ_U is the exponential decay rate of the flow speed U. The fitting used the time points for which U^2 had not yet reached values below $e^{-3} \approx 5\%$ of its maximum.

The scan over k_x was done by varying the mode number according to $N \in \{1, 2, ..., 7\}$, using simulation time $t_\mathrm{max} = 27000$ for $N = 1 - 4$ and $t_\mathrm{max} = 5400$ for $N = 5 - 7$, while keeping $k_{0,e} = k_{0,i} = 2\pi$ fixed. The results of two representative cases in the scan, $N = 1$ and $N = 7$, are shown in figure 4.1. As predicted the flow decays exponentially, and the linear fits appear to represent the data well.

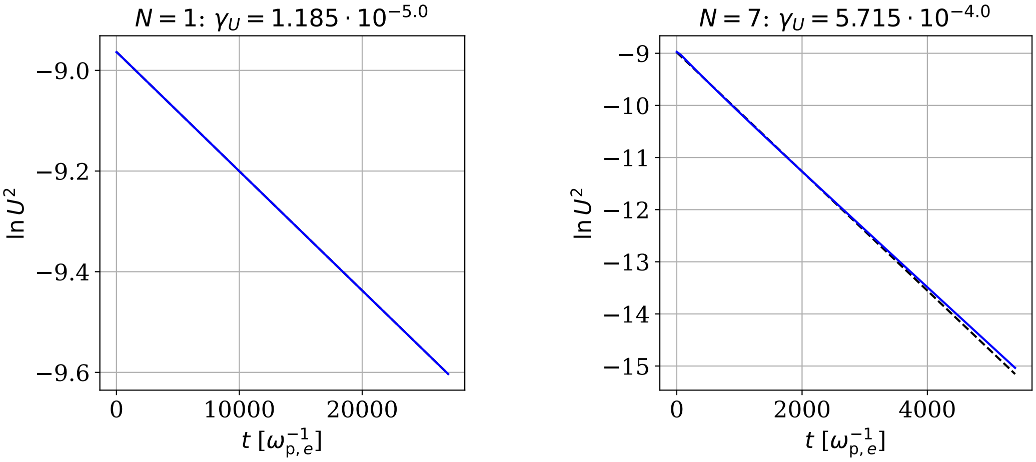

(a) **(b)**

Figure 4.1: Simulated flow decay (blue) and a linear fit to $\ln(U^2)$ as a function of time (black dashed) for two of the cases in the k_x-scan using the isotropization closure: (a) $N = 1$, (b) $N = 7$. Note the different scales on the y-axes.

The flow decay rate γ_U was calculated for each flow wave number in the scan, and the dependence of $\ln \gamma_U$ on $\ln k_x$ is visualized in figure 4.2. A linear is fitted to the data points in this figure, noting that the dependence of γ_U on k_x obeys a power law quite accurately, which gives the dependence $\gamma_U \sim k_x^{1.986}$. Given that the exponent is close to the integer 2, it can be predicted that the flow decay rate depends on k_x as $\gamma_U \sim k_x^2$ in theory, when approaching a physical ion-electron mass-ratio.

Choosing $N = 3$ to fix k_x, the ion closure parameter was varied according to $k_{0,i} \in \{0.2\pi, 0.4\pi, \pi, 2\pi, 4\pi, 10\pi, 20\pi\}$, while keeping $k_{0,e} = 2\pi$. For the smallest two values of $k_{0,i}$ a simulation time of $t_\mathrm{max} = 5400$ is used, and $t_\mathrm{max} = 27000$ is used for the rest. The results for the representative cases $k_{0,i} = 0.4\pi$ and $k_{0,i} = 10\pi$ are shown in figure 4.3. For most cases in the scan, the decay deviates slightly from being exponential, as can be seen in the linear fit not being in perfect agreement with the data in the $k_{0,i} = 10\pi$ case in figure 4.3b.

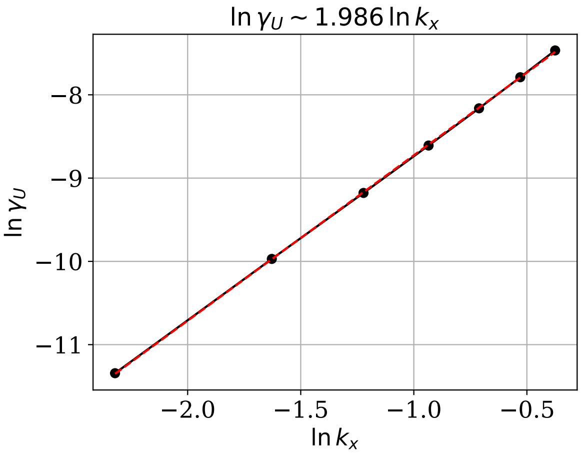

Figure 4.2: The dependence of the flow decay rate γ_U on k_x for all cases in the scan (black) using the isotropization closure, and a linear fit to $\ln\gamma_U$ as a function of $\ln k_x$ (red dashed).

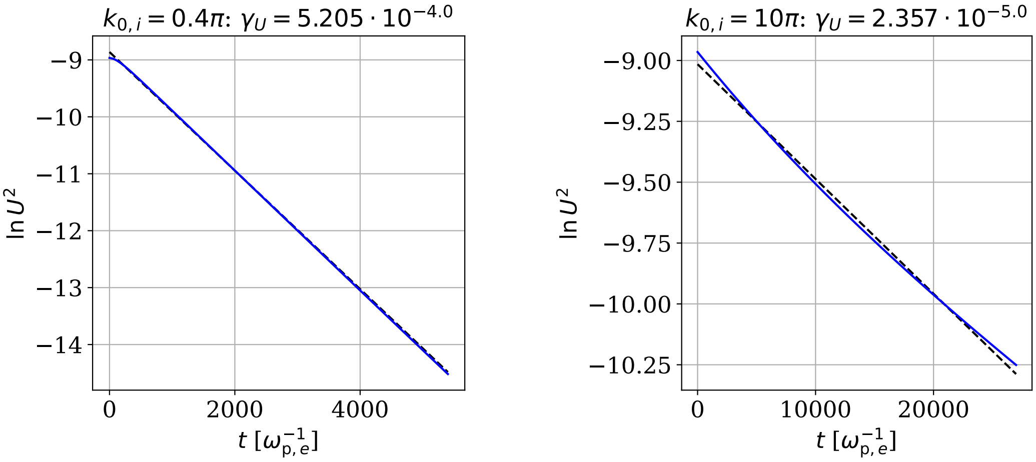

(a) **(b)**

Figure 4.3: Simulated flow decay (blue) and a linear fit to $\ln(U^2)$ as a function of time (black dashed) for two of the cases in the $k_{0,i}$-scan using the isotropization closure: (a) $k_{0,i} = 0.4\pi$, (b) $k_{0,i} = 10\pi$. Note the different scales on the y-axes.

The dependence of $\ln\gamma_U$ on $\ln k_{0,i}$ is illustrated in figure 4.4 using the decay rates calculated for each case in the $k_{0,i}$-scan. Using a linear fit to the data points in this figure gives the dependence $\gamma_U \sim k_{0,i}^{-0.951}$. Noting again that this exponent is close to an integer, the flow decay rate likely depends on $k_{0,i}$ as $\gamma_U \sim k_{0,i}^{-1}$ in theory as the mass-ratio between ions and electrons approaches the physical mass-ratio.

Finally, the electron closure parameter was scanned over by varying it according to $k_{0,e} \in \{0.2\pi, 0.4\pi, \pi, 2\pi, 4\pi, 10\pi, 20\pi\}$, while keeping k_x fixed by setting $N = 3$ and fixing $k_{0,i} = 2\pi$. The simulation time $t_{\max} = 27000$ was used for all cases in this

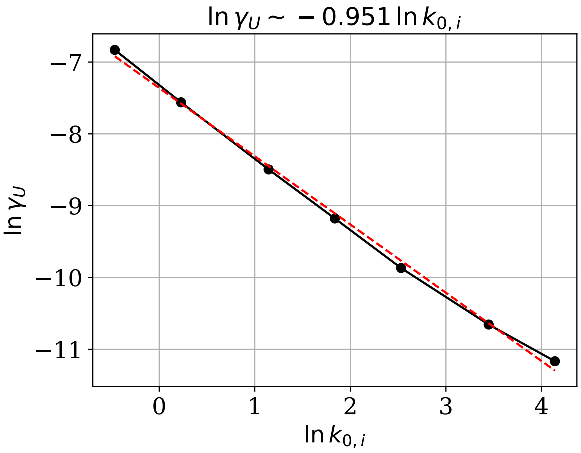

Figure 4.4: The dependence of the flow decay rate γ_U on $k_{0,i}$ for all cases in the scan (black) using the isotropization closure, and a linear fit to $\ln \gamma_U$ as a function of $\ln k_{0,i}$ (red dashed).

scan. Performing the same analysis as for the previous scans, the flow decay rate γ_U is calculated using linear fitting for each case and the resulting dependence of $\ln \gamma_U$ on $\ln k_{0,e}$ is shown in figure 4.5. The dependence of the flow decay rate γ_U on $k_{0,e}$ is very weak as compared to the dependencies on $k_{0,i}$ and k_x — only $\gamma_U \sim k_{0,e}^{0.015}$, where the closest integer exponent would be 0. This means that the mass flow, dominated by the ions, is practically independent of the electron closure, which reflects the separation of electron and ion physics expected for non-pair plasmas. In summary, the effective fluid Reynolds number is thus found to scale approximately as $Re \sim k_{0,i}/k_x^2$, according to equation (3.10), for the isotropization closure.

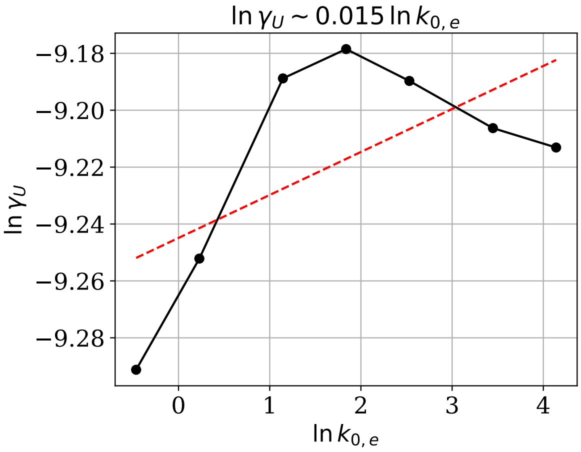

Figure 4.5: The dependence of the flow decay rate γ_U on $k_{0,e}$ for all cases in the scan (black) using the isotropization closure, and a linear fit to $\ln \gamma_U$ as a function of $\ln k_{0,e}$ (red dashed).

In figure 4.5 it is evident that the low sensitivity of γ_U to $k_{0,e}$ results in an uncertainty in the exact relation between γ_U and $k_{0,e}$ — it is not a clear power law dependence. Generally, the cases with high values of $k_{0,e}$ displayed a close to exponential flow decay, while the other cases were further from perfectly exponential.

4.2.1.1 Theoretical Ion Flow Damping Rate

The ion flow damping rate should in theory coincide with the MHD flow damping rate if ion and electron dynamics are sufficiently decoupled. This appears to be the case, since the MHD flow decay rate was found in section 4.2.1 to barely depend on the electron closure parameter for the ion-electron mass-ratio employed here. A theoretical prediction of the ion flow damping rate, for comparison with the dependencies on $k_{0,i}$ and k_x obtained for the MHD flow damping rate presented in section 4.2.1 can be found in the manner presented in this section.

The terms of the ion momentum and energy equations (equations (2.17) and (2.18)), for components z and xz respectively, were calculated from the output data of the flow decay case with $N = 3$, $k_{0,e} = k_{0,i} = 2\pi$, at the time point $t = 3000\,\omega_{\mathrm{p},e}^{-1}$. These are the most interesting components, since u_z was the initial non-zero component of the velocity and the x-direction is the direction in which quantities can have non-zero spatial derivatives. Numerical derivatives were taken in x and t, centered with spatial step $2\mathit{\Delta} x$ and time step $2\mathit{\Delta} t_{frame}$, where $\mathit{\Delta} t_{frame}$ is the time resolution of the saved output data. The calculated terms are shown in figures 4.6a and 4.6b along with the sums of the left and right hand side terms. The thermal velocity $v_{\mathrm{th},i}$ was calculated as $\sqrt{T_i/m_i}$ in the energy equation, in accordance with the conventions used in `Gkeyll`, matching the left- and right-hand sides of the equation.

In the equation for the ion pressure tensor, it is seen in figure 4.6b that the terms that dominate and almost balance each other are the closure term $v_{\mathrm{th},i}k_{0,i}\mathsf{p}_{i,xz}$ and the term $\mathsf{p}_{i,xx}\partial_x u_{i,z}$. That is, the off-diagonal ion pressure created by the sheared flow is almost completely removed by the closure term. In the momentum equation, figure 4.6a shows that the terms $m_i n_i \partial_t u_{i,z}$ and $\partial_x \mathsf{p}_{i,xz}$ dominate, thus the deceleration is caused by the only non-zero off-diagonal tension force. These four terms are therefore the most important. Considering a slightly more general situation — including the dominating terms found in these equations as well as any terms containing a time derivative — for the z- and xz-components, a quadratic equation can be derived for the ion flow damping rate γ_i. This is achieved by taking the ansatz:

$$\begin{aligned} u_{i,z} &= u_{i,z,0}\exp(-\gamma_i t)\cos(k_x x) \\ \mathsf{p}_{i,xz} &= \mathsf{p}_{i,xz,0}\exp(-\gamma_i t)\cos(k_x x - \varphi), \end{aligned} \tag{4.3}$$

where it turns out that $\varphi = \pi/2$, given that $\gamma_i > 0$ and that n_i does not vary significantly with x. Also assuming that the system remains close to thermodynamic equilibrium, $\mathsf{p}_{i,xx} \approx p_i$, yields the solutions

$$\gamma_i = \frac{v_{\mathrm{th},i}k_{0,i}}{2}\left(1 \pm \sqrt{1 - 4\frac{k_x^2}{k_{0,i}^2}}\right) = \left\{k_{0,i} \gg k_x\right\} \approx \begin{cases} v_{\mathrm{th},i}k_{0,i}\left(1 - \frac{k_x^2}{k_{0,i}^2}\right) \\ v_{\mathrm{th},i}\frac{k_x^2}{k_{0,i}} \end{cases} \tag{4.4}$$

to this quadratic equation. See appendix A for a detailed derivation of these solutions.

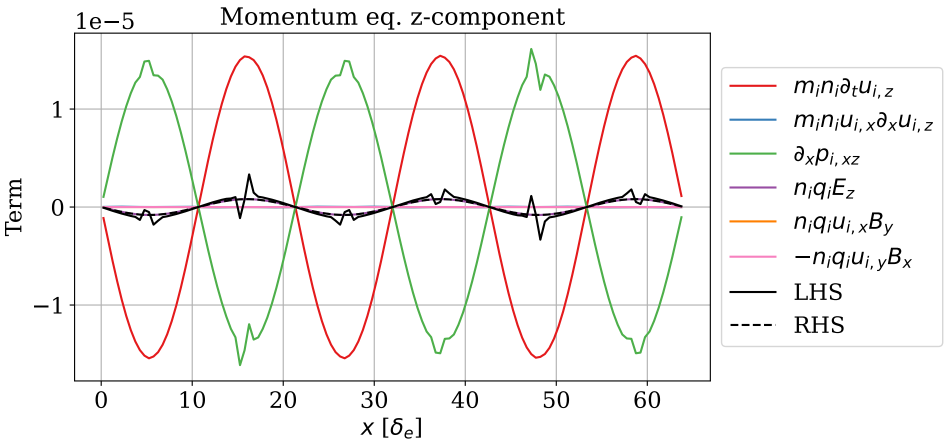

(a)

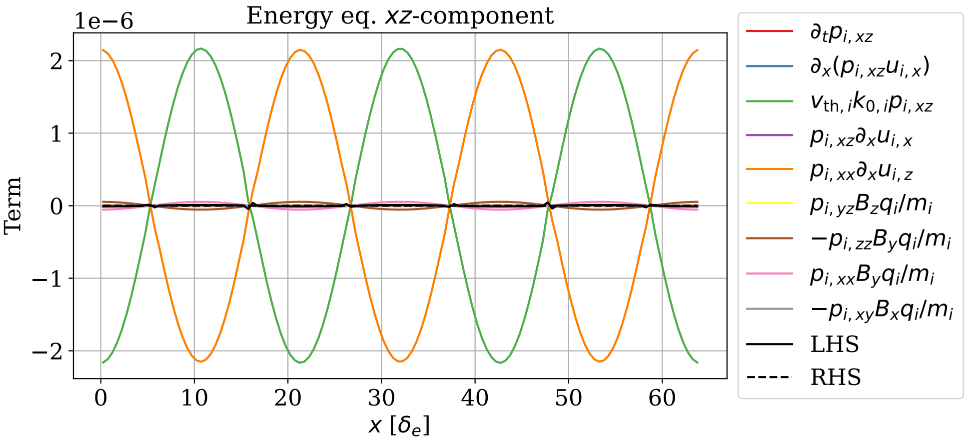

(b)

Figure 4.6: Numerical evaluation of all terms, as well as left- and right-hand side sums, of the z- and xz-components of the ion (a) momentum and (b) energy equations. The data corresponds to the $N = 3$, $k_{0,e} = k_{0,i} = 2\pi$ flow decay case with the isotropization closure, at the time point $t = 3000\,\omega_{\mathrm{p},e}^{-1}$.

In the k_x-scan, where $k_{0,i} = 2\pi = 6.283$ was kept fixed, the largest k_x was obtained with $N = 7$, for which $k_x = 0.687$. In the $k_{0,i}$-scan k_x was kept fixed to $k_x = 0.295$ ($N = 3$), and the smallest $k_{0,i}$-value was $k_{0,i} = 0.2\pi = 0.628$. Therefore, a majority of cases in the two scans are firmly in the $k_{0,i} \gg k_x$ limit, and one of the solutions (4.4) should be applicable. Noting that γ_U increases with k_x in figure 4.4, the second solution should be correct. Comparing the dependencies found in the scans for the MHD flow decay rate, $\gamma_U \sim k_x^{1.986}/k_{0,i}^{0.951}$, to the dependencies of the derived analytical solution for the ion flow decay rate, $\gamma_i \sim k_x^2/k_{0,i}$, these are notably consistent. The fact that the electron fluid equations were not considered in the derivation of the analytical dependencies, while still obtaining a solution consistent with the numerical results, confirms that the flow decay rate sensitivity to electron dynamics is very low and that ion and electron dynamics are substantially separated at the employed mass-ratio.

A similar exercise as in this section, while in principle possible, is not performed for the magnetic field damping, since it would be significantly more complicated due to the intricate coupling between the field and fluid equations.

4.2.2 Magnetic Field Decay

In the magnetic field decay simulations the values of B^2 at each saved time point were calculated and integrated over the simulation box. The result is denoted by B^2 in this section. In the same manner as for the flow decay, linear fitting was used to find the decay rate γ_B of B. The linear fit to $\ln(B^2)$ as a function of t used only the time points for which B^2 was larger than $e^{-3} \approx 5\%$ of its maximum.

The same type of scans as for the flow decay were done for the magnetic field decay setup. A first scan over k_x was again done by varying the mode number $N \in \{1, 2, ..., 7\}$, while keeping $k_{0,e} = k_{0,i} = 2\pi$ fixed. Simulation times were set to $t_{\max} = 27000$ for $N = 1 - 4$ and $t_{\max} = 5400$ for $N = 5 - 7$. Two representative cases in the scan, $N = 1$ and $N = 7$, are shown in figure 4.7. When the values of B^2 get very small, like in figure 4.7b, the decay starts to deviate from being strictly exponential. This was the primary reason for why linear fitting was done for "early" time points, where the major part of the decay takes place.

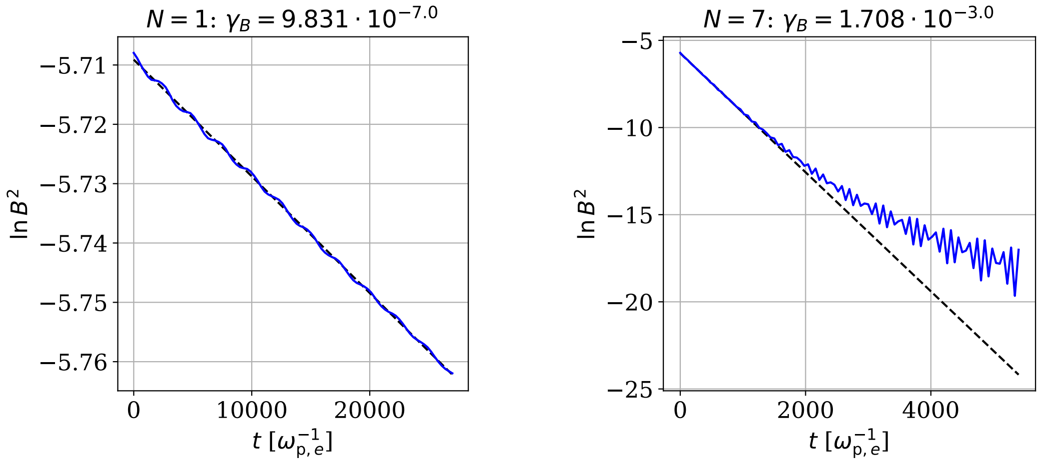

(a) **(b)**

Figure 4.7: Simulated magnetic field decay (blue) and a linear fit to $\ln(B^2)$ as a function of time (black dashed) for two of the cases in the k_x-scan using the isotropization closure: (a) $N = 1$, (b) $N = 7$. Note the different scales on the y-axes.

The magnetic field decay rate was calculated for each case in the scan, and in figure 4.8 the obtained values of $\ln \gamma_B$ are plotted as a function of $\ln k_x$. A linear fit to this curve gives the approximate dependence $\gamma_B \sim k_x^{3.843}$ of the decay rate on the wave number. This dependence is thus very strong compared to the other dependencies found, and as shall be seen later, it has an important impact on the magnetic spectra in dynamo simulations. It can be expected that the theoretical limit of the exponent at large ion-electron mass-ratios would be the integer 4.

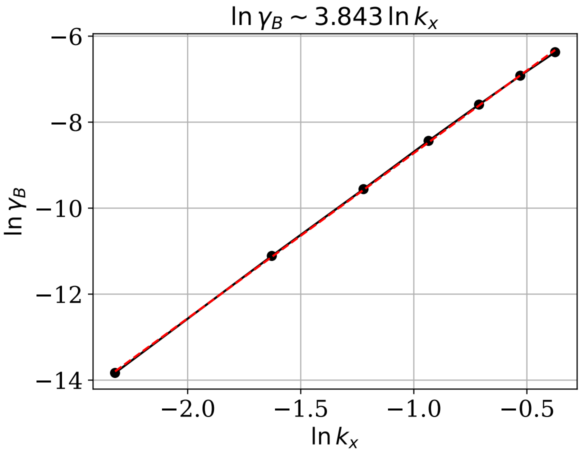

Figure 4.8: The dependence of the magnetic field decay rate γ_B on k_x for all cases in the scan (black) using the isotropization closure, and a linear fit to $\ln \gamma_B$ as a function of $\ln k_x$ (red dashed).

The $N = 3$, $k_{0,i} = 2\pi$ case above was chosen as the basis of the $k_{0,e}$-scan for the magnetic field decay. The electron closure parameter was varied according to $k_{0,e} \in \{0.2\pi, 0.4\pi, \pi, 2\pi, 4\pi, 10\pi, 20\pi\}$ using the simulation time $t_{\max} = 27000$. Two representative cases, $k_{0,e} = \pi$ and $k_{0,e} = 20\pi$, are presented in figure 4.9. It is worth noting that in figure 4.9a, and for low $k_{0,e}$-values in general, there seems to be another decay mode of B^2 that starts to dominate at weak field strengths (large enough time), below $B^2 \approx e^{-10}$. An investigation into the origin of this second decay mode showed that its appearance coincides with situations when the ion current has grown comparable to the electron current. Since driving an ion current is increasingly more difficult compared to driving an electron current for high mass-ratios, this second decay mode is likely not relevant at physical mass-ratios.

Plotting $\ln \gamma_B$ for the calculated decay rates in each case of the $k_{0,e}$-scan as a function of $\ln k_{0,e}$ in figure 4.10, and fitting a linear to the data, the dependence $\gamma_B \sim k_{0,e}^{-0.893}$ is obtained. It is noteworthy that the decay rate of B depends on $k_{0,e}$ in a similar way that the decay rate of U depends on $k_{0,i}$, both exponents being close to the integer -1.

Taking the case with $N = 3$, $t_{\max} = 27000$ and $k_{0,e} = 2\pi$, $k_{0,i}$ was varied using the same scan values as for $k_{0,e}$ previously. Generally, larger values of $k_{0,i}$ showed a stronger deviation from strict exponential decay than the smaller values. However, the dependence of the calculated decay rate of B on the ion closure parameter $k_{0,i}$ was found to be weak — only $\gamma_B \sim k_{0,i}^{-0.037}$ — see figure 4.11. This is reminiscent of the flow decay rate's dependence on $k_{0,e}$, which was also so weak that the closest integer power-law exponent for the dependence was 0. To summarize, the effective

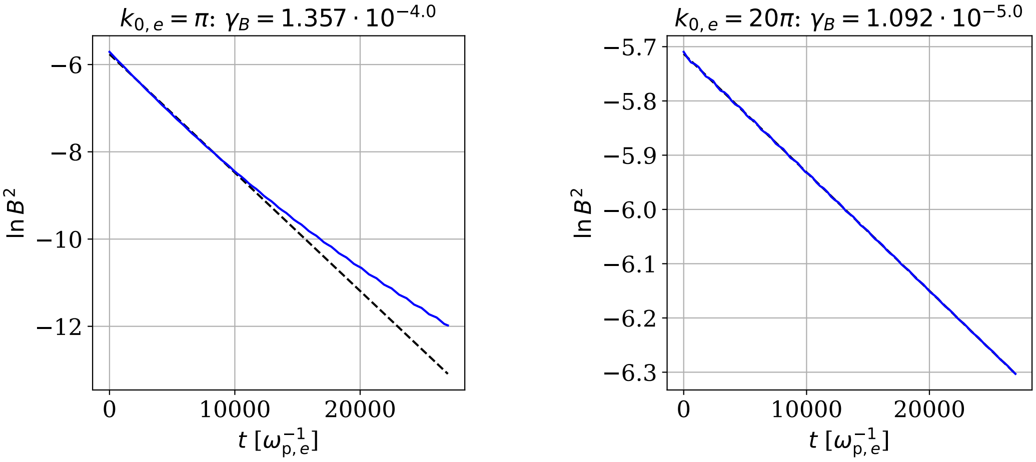

(a) **(b)**

Figure 4.9: Simulated magnetic field decay (blue) and a linear fit to $\ln(B^2)$ as a function of time (black dashed) for two of the cases in the $k_{0,e}$-scan using the isotropization closure: (a) $k_{0,e} = \pi$, (b) $k_{0,e} = 20\pi$. Note the different scales on the y-axes.

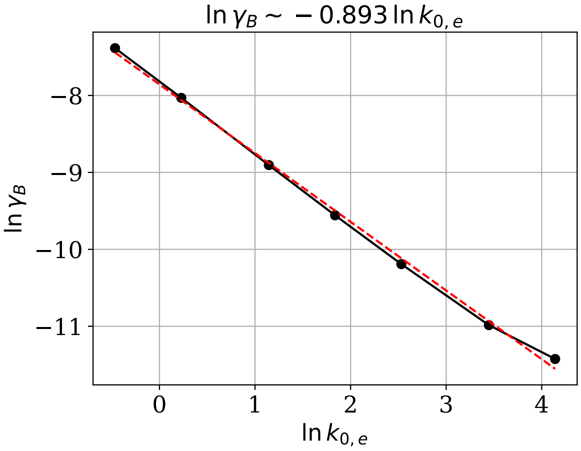

Figure 4.10: The dependence of the magnetic field decay rate γ_B on $k_{0,e}$ for all cases in the scan (black) using the isotropization closure, and a linear fit to $\ln \gamma_B$ as a function of $\ln k_{0,e}$ (red dashed).

magnetic Reynolds number is thus found to scale approximately as $Rm \sim k_{0,e}/k_x^4$, according to equation (3.9), for the isotropization closure.

The electron and ion closure parameters have in practice no effect on the flow damping and magnetic field damping respectively, which can be contrasted to their significant impacts on the dynamics of their respective particle species, demonstrated by the approximate $\gamma_U \sim k_{0,i}^{-1}$ and $\gamma_B \sim k_{0,e}^{-1}$ dependencies found. Evidently the mass-ratio $m_i/m_e = 100$ that is used in the simulations is significant enough to mostly

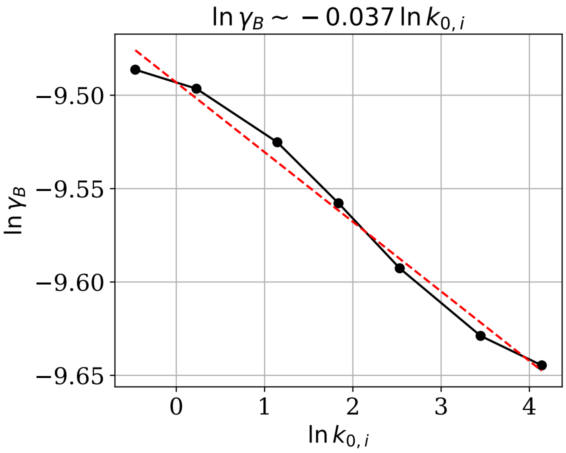

Figure 4.11: The dependence of the magnetic field decay rate γ_B on $k_{0,i}$ for all cases in the scan (black) using the isotropization closure, and a linear fit to $\ln \gamma_B$ as a function of $\ln k_{0,i}$ (red dashed).

separate electron and ion dynamics, so that these can each dominate in different scenarios.

4.2.2.1 Increased Ion-Electron Mass-Ratio

It can be expected that the dependence of γ_B on k_x should be an integer in the high ion-electron mass-ratio limit, since the ions would then be essentially stationary compared to the electrons, and only the electron 10-moment equations would have to be solved. To study what happens with the k_x-dependence of γ_B at 10 times higher mass-ratio, $m_i = 1000 m_e$, the same simulations were run as in the k_x-scan for $N = 1, 2, 3, 4$ with the larger mass-ratio. This results in the dependence $\gamma_B \sim k_x^{3.918}$ as shown in figure 4.12. As expected the power-law exponent is closer to the nearest integer exponent, 4, than when using the lower mass-ratio, where the exponent was 3.843.

4.3 Gradient-Based Closure

Similarly to the previous studies using the relaxation closure, an attempt to obtain similar scaling expressions for the magnetic field and the ion flow damping was made using the gradient-based closure (equation (3.15)). The behavior found is significantly more complex than what could be represented by a simple exponential damping ansatz, and the physicality of the obtained results is questionable. To nevertheless illustrate the obtained behavior, some representative examples of simulations using the same initial conditions as before will be demonstrated in this section.

When using the gradient-based closure, the resulting flow and magnetic field evolution in the two different scenarios turned out to not follow the expected exponential

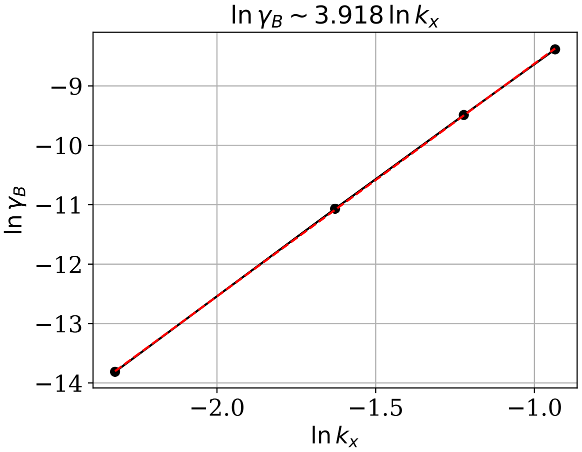

Figure 4.12: The dependence of the magnetic field decay rate γ_B on k_x for the cases $N = 1, 2, 3, 4$ (black) using the isotropization closure and an increased mass-ratio of $m_i/m_e = 1000$, and a linear fit to $\ln \gamma_B$ as a function of $\ln k_x$ (red dashed).

decay. Instead, the general behavior of U^2 and B^2 was oscillatory with — not simply exponentially — decaying envelopes. In certain cases the decay ceased and stabilized the quantity around some finite value, and in others the decay would be significant enough for the quantity to reach very small values, only to then sometimes grow quickly again — also stabilizing around some finite value. The physical quantities in these simulations also displayed “mode decay”, that is better represented by considering the time evolution of the individual spatial Fourier modes. Studying the initially sinusoidal B_y or U_z that corresponded to a certain wave number $k_{x,in}$, these quantities would over time change their characteristic wavelength and corresponding k_x. This trend became more and more prominent with higher initial mode numbers N_{in} for the sinusoidally varying U_z and B_y, where N_{in} would “decay” to lower mode numbers — the characteristic wavelength of the sinusoidal quantities increased with time.

Simulations with various settings for N_{in}, $k_{0,e}$ and $k_{0,i}$ similar to those done for the isotropization closure in section 4.2 were done with both the flow and magnetic field decay setup, using a long simulation time of $t_{\text{max}} = 18000$. To study which mode dominates at different times the spatial Fourier transform in x was taken of the non-trivial component of the relevant quantity (B_y or U_z), from which the power spectrum could be calculated. The Fourier modes and mode numbers are denoted $k_{x,\text{FT}}$ and N_{FT} respectively, and obey $k_{x,\text{FT}} \approx 0.098 N_{\text{FT}}$. Modes that at any time point were within 1% of the power spectrum's maximum at that time were included in figures where $\ln |\mathcal{F}(B_y)|^2$ or $\ln |\mathcal{F}(U_z)|^2$ is plotted against time in order to find decay rates of the different modes.

Cases with low initial mode numbers show relatively simple behavior, with only the initial mode active throughout the simulation, decaying approximately exponentially with some overlying oscillations at long timescales. The magnetic field decay cases also display a sharp initial decay before the long-time exponential decay starts. For larger initial mode numbers, corresponding to $N_{\text{in}} = 4 - 7$, some mode decay can be observed. Representative examples for the flow and magnetic field decay scenarios, using $k_{0,i} = k_{0,e} = 2\pi$, are shown in figures 4.13 (using $N_{\text{in}} = 7$) and 4.14 (using $N_{\text{in}} = 5$) respectively. The linear fits that are used to estimate decay rates γ_B and γ_U for the different modes are fitted to the last half of the simulation time points in the magnetic field decay case, and to the $t \in [0.1t_{\max}, 0.5t_{\max}]$ range in the flow decay case. This choice was based on the time ranges in which the modes showed a behavior best estimated by an exponential decay. Here the slope of the natural logarithm of the power spectrum as a function of time is defined to have the slope $-2\gamma_{B/U}$. As observed in figure 4.14, the "jumps" between finite values of B^2 correspond to mode decay.

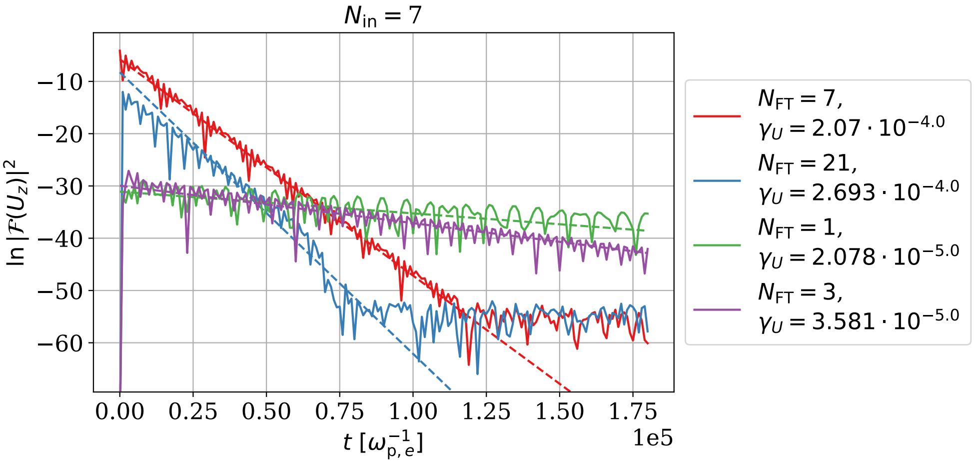

Figure 4.13: The time evolution of dominant modes in the power spectrum of U_z (solid) and linear fits to $\ln|\mathcal{F}(U_z)|^2$ as a function of time for each included mode (dashed), for the flow decay setup using the gradient closure, $k_{0,e} = k_{0,i} = 2\pi$ and $N_{\text{in}} = 7$. The given values of γ_U correspond to the calculated decay rates of each mode.

Since periodic boundary conditions on the simulation box are enforced in the x-direction, only mode numbers corresponding to whole numbers N, with modes $k_x = 2\pi N/L_0$, are allowed. However, tests were done of what happens when doubling the size of the simulation box to $2L_0$ (while keeping the resolution fixed). Because of the periodic boundary conditions now not being implemented at $x = L_0$, the active modes could be $k_x = 2\pi N/(2L_0)$, corresponding to half or whole mode numbers $N/2$. Because of this fact, a lot more modes were present in cases displaying mode decay when doubling the box size. The physicality of the results is therefore questionable.

Because the scaling of the decay rate with N is non-trivial, and that in many cases there is no clear decay rate that can be determined, the behavior of the system when using the gradient-based closure is difficult to interpret physically. For the reason that this closure does not seem to work well in these types of simulations, as physically questionable results are obtained, it was decided that the gradient-based

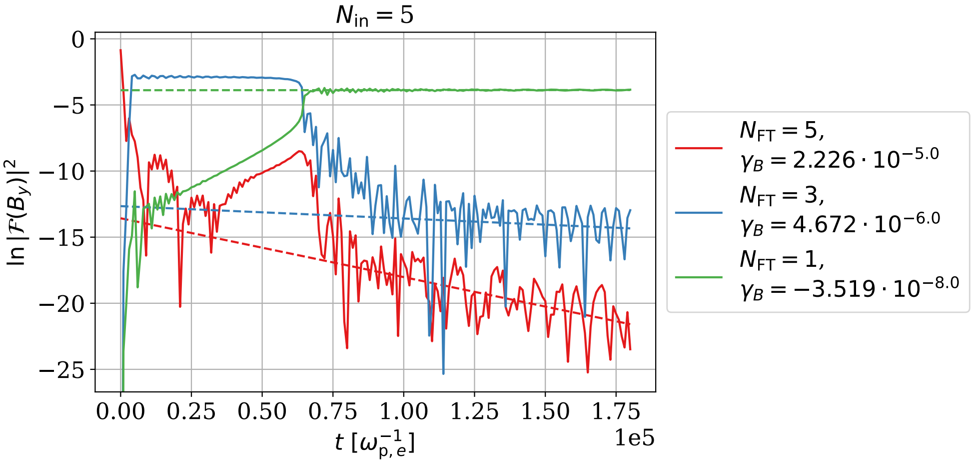

Figure 4.14: The time evolution of dominant modes in the power spectrum of B_y (solid) and linear fits to $\ln|\mathcal{F}(B_y)|^2$ as a function of time for each included mode (dashed), for the magnetic field decay setup using the gradient closure, $k_{0,e} = k_{0,i} = 2\pi$ and $N_{\text{in}} = 5$. The given values of γ_B correspond to the calculated decay rates of each mode.

closure would not be used in the three-dimensional dynamo simulations in chapter 5.

It should, however, be noted that there are scenarios in which the gradient-based closure performs reasonably well, even compared to kinetic simulations, such as in magnetic reconnection setups [45]. The gradient-based closure is a generalization of one of Fick's laws, $\boldsymbol{q} \propto -\nabla T$, where T is a scalar temperature and $\boldsymbol{q}$ is a heat flux vector, to the situation when both the heat flux and temperature are tensors. There is not a unique way of such generalization, and under certain physical conditions a certain choice may perform better or worse.

5

Collisionless Fluid Dynamo Simulations

In this chapter the setup and results of the three-dimensional collisionless dynamo simulations, where a simulation box-scale GP-flow is driven through the system, are presented. The aim is to perform a scan over the electron closure parameter $k_{0,e}$, using the isotropization closure for the heat flux tensor in the 10-moment equations (2.16), (2.17) and (2.18), in order to study the effect of magnetic field damping strength on dynamo action in collisionless plasmas.

Having found the dependence $\gamma_B \sim k_{0,e}^{-1}$ of the magnetic field damping rate on $k_{0,e}$ in section 4.2.2, the generalized magnetic Reynolds number depends on the closure parameter as $Rm \sim k_{0,e}$ according to equation (3.9). A scan over $k_{0,e}$ is therefore analogous to a scan over the magnetic Reynolds number in the classical MHD dynamo treatment. As shall be seen, there are, however, important differences between scanning over the closure parameter and the MHD magnetic Reynolds number.

As will be observed and analyzed in section 5.2, rapid magnetic field seed generation due to the pressure anisotropy-driven Weibel instability also plays a major role in these simulations. The ability to evolve the entire pressure tensors of both electrons and ions is an important feature of the `Gkeyll` 10-moment fluid solver that classical MHD codes lack, and allows for retaining such pressure anisotropy-driven instabilities.

5.1 Simulation Setup

In the three-dimensional dynamo simulations the simulation setup is done in SI-units. The overall settings are based on those of the fluid simulation of a dynamo presented in [49], that also used `Gkeyll`:s 10-moment collisionless fluid solver.[1] The initial number densities of both the electron and ion populations are set to $n_\alpha = 2.302 \cdot 10^{28}\,\mathrm{m}^{-3}$, their temperatures to $T_\alpha = 1\,\mathrm{keV}$ and their pressure tensors are taken to be isotropic with the scalar pressure $p_\alpha = n_\alpha T_\alpha$. Just like in the scans of magnetic field and flow decay in chapter 4, a reduced ion-electron mass-ratio of $m_i/m_e = 100$ is used, and the ions are taken to be singly charged. The simulation box is taken to

---

[1] That simulation used an older version of `Gkeyll` with different features and numerical schemes.

be of length $L_0 = 24.32\,\mu\text{m}$ in each direction. That the absolute values of density and spatio-temporal scales — chosen to be similar to previous studies — are far from being representative of the intracluster medium is not a major concern. This is because the collisionless Vlasov-Maxwell system can be rigorously re-scaled to larger scales and lower densities, such that the dynamics of the re-scaled system is essentially identical [50]. This fact provides the basis of laboratory astrophysics.

A GP-flow $\boldsymbol{U}_{\text{GP}}(t = 0, \boldsymbol{x})$, defined according to equation (3.4) with $A = C = 1$, is used as the initial condition for the velocities of the ions. The electrons were initiated with a fluid velocity formed by the same GP-flow as for the ions, with an added velocity contribution from the current corresponding to the initialized seed magnetic field. The characteristic length scale and speed of the flow are set to L_0 and $u_0 = M_0 c_s = 4.642 \cdot 10^5\,\text{m/s}$ respectively, where M_0 is the Mach number and $c_s = \sqrt{T_e/m_i}$ is the sound speed. Observationally, flows are usually subsonic [51], so the aim was to not include the effects of sonic flows, which can lead to shocks, in these simulations. Following the settings used for the fluid dynamo simulation in [49], the targeted Mach number was therefore set to $M_0 = 0.35$. Since the simulation box has side length L_0, the wave number $k_0 = 2\pi/L_0$ used in the sinusoidal GP-flow is also the lowest (positive) spatial Fourier mode of the simulation box. Note that this k_0 is different from the closure parameters $k_{0,\alpha}$.

In a particle-in-cell (PIC) code seed noise for instabilities is naturally present due to the statistical noise from the discreteness of particles, but some initial magnetic field noise needs to be specified for the dynamo simulations using the 10-moment fluid solver of `Gkeyll`, since it is otherwise completely noise free. Initially, the magnetic field is defined as

$$\boldsymbol{B} = B_0 \sum_{i \neq j, n} b_{ij,n} \cos(n k_0 (x_i + \varphi_{ij,n})), \tag{5.1}$$

where the noise amplitude is taken to be $B_0 = 1\,\text{T}$, $i, j = 1, 2, 3$ are component indices and $n = 1, 2, ..., N$ is the mode number. The number of modes included is set to $N = 4$. The relative amplitudes $b_{ij,n}$ and the phases $\varphi_{ij,n}$ are chosen at random, uniformly, in the range $[0, 1]$. The electric field is initialized to $\boldsymbol{E} = 0$, and the current density to $\boldsymbol{j} = \nabla \times \boldsymbol{B}/\mu_0$, initially carried by the electrons, with $\boldsymbol{B}$ as defined in equation (5.1).

Some timescales relevant to the problem are the turnover time, defined as $t_{\text{turnover}} = L_0/u_0$, and the ion streaming time, $t_{\text{stream},i} = L_0/v_{\text{th},i}$. Comparing these to the inverse electron plasma frequency, the relations $t_{\text{turnover}} = 4.041\, t_{\text{stream},i} = 4.484 \cdot 10^5\, \omega_{\text{p},e}^{-1} = 5.239 \cdot 10^{-11}\,\text{s}$ are obtained.

A continuous forcing is applied during the simulation in order to drive the flow, where the force on the particles is defined as

$$\boldsymbol{F}_\alpha = C_f m_\alpha \boldsymbol{U}_{\text{GP}}(t, \boldsymbol{x}) / t_{\text{stream},i}, \tag{5.2}$$

such that the applied accelerations on both particle species are equal. Here the dimensionless factor C_f is called the force factor, and is set to take the value 2 as the default. The settings for the GP-flow used here are the same as the ones used in the $\boldsymbol{U}_{\text{GP}}$ initial condition for the species' velocities, except that it now evolves with time. The time oscillations of the GP-flow are taken to have the angular frequency $\omega = 2\pi/t_{\text{turnover}}$.

Periodic boundary conditions on the simulation box are used in all three spatial directions, and the volume is divided into 64^3 cells in total by using $N_{x,y,z} = 64$ grid points in each direction. The spatial resolution that could be used was limited by the available computational resources. The time resolution is given by choosing the three-dimensional CFL-condition [47, 48] to be exactly fulfilled. The default value of the total simulation time was taken to be $t_{\text{max}} = 12.374\, t_{\text{turnover}}$, and output data was saved for a minimum of 113 time steps, including the initial step. The minimal time resolution for saving output data, used during the later parts of the simulations, was $\Delta t_{frame} = 0.1650\, t_{\text{turnover}}$, which would be equivalent to the resolution if the entire time range was saved at 76 uniformly distributed time points (including the initial time point).

As established in section 4.3, the gradient-based closure is physically questionable in these types of simulations, so only the isotropization closure (equation (3.14)) is used in the dynamo simulations. The value of the ion closure parameter is chosen as $k_{0,i} = 85.33/L_0$. A scan over the electron closure parameter was performed, where $k_{0,e}$ was varied in the range $2\pi/(2^{-m}L_0)$ for $m = 0, 1, ..., 7$. The smallest $k_{0,e}$-value therefore corresponds to a wavelength of box size L_0, and the largest to a wavelength $\Delta x/2$, smaller than grid scale Δx and therefore unresolved. Note though that the closure parameter, while having the dimension of a wavenumber, is just a parameter affecting the pressure tensor locally, and therefore not resolving the corresponding length scale is not a concern.

5.2 Weibel Instability Analysis

The first case in the scan over the electron closure parameter $k_{0,e}$ for the isotropization closure uses $k_{0,e} = 2\pi/L_0$, so that the wavelength corresponding to this wave number is the box size, and the characteristic length scale of the GP-flow, L_0. Shown in figure 5.1 is the time evolution of the magnetic and flow energies, as well as the magnetic energy spectrum, obtained in this case. As clearly illustrated in figure 5.1a, a considerable fraction of the magnetic energy growth in the simulation takes place on a timescale significantly shorter than the turnover time, which should be the characteristic timescale of a developing dynamo. Such behavior has not been observed in previous MHD dynamo studies. Therefore, this rapid growth is suspected to occur not due to the dynamo effect, but due to some plasma instability that can be modeled in the fluid simulation framework. Most likely this has to do with all components of both the electron and ion pressure tensors being evolved in `Gkeyll`, so that pressure anisotropies can develop and in turn activate pressure anisotropy-driven instabilities for each species.

It is suspected that the rapid magnetic field growth observed for this case occurs due to the pressure anisotropy-driven Weibel instability. In [5] kinetic particle-in-cell dynamo simulations of pair plasmas are performed, and notably, the evolution of the magnetic and flow energies in figure 5.1a are qualitatively similar to those of

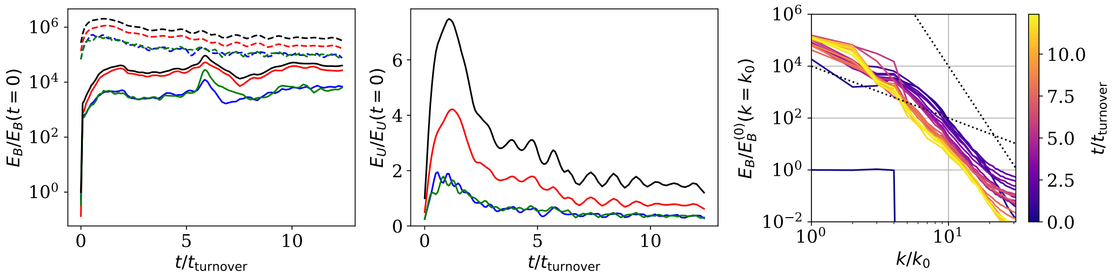

(a) **(b)** **(c)**

Figure 5.1: The $k_{0,e} = 2\pi/L_0$ case of the electron closure parameter scan. (a) Time evolution of the magnetic energy (solid) and the flow energy (dashed), both normalized to the magnetic energy at $t = 0$. The total energies are shown in black, and the contributions to the energy from the three vector components in the x, y, z-directions are shown in red, blue and green respectively. (b) The total flow energy (black), and its contribution from the three vector components in the x, y, z-directions (red, blue, green), all normalized to its initial value. (c) The magnetic energy spectrum normalized to its value at $k = k_0$ and $t = 0$, for 25 time points approximately uniformly distributed in the range $t/t_{\mathrm{turnover}} \in [0, t_{\mathrm{max}}]$, where the curve color corresponds to the time. Shown in dotted black are k^{-2} and k^{-8}, for reference.

the inverse plasma beta β^{-1} and the square of the Mach number M^2 (essentially the magnetic and flow energies normalized to the scalar pressure) shown in their figure 2. Like in figure 2 of [5], the magnetic energy in figure 5.1a shows rapid initial growth, but remains smaller than and does not quite reach equipartition with the flow energy, even over long timescales. It is established in this paper that the growth of the magnetic energy on timescales much smaller than those expected of a flow-driven dynamo arises from the electron Weibel instability (though it should be noted that in pair-plasmas there are not separate ion and electron Weibel instabilities), which leads to the prediction that the Weibel instability is active in the simulation presented in figure 5.1 as well.

To determine whether its cause is indeed the Weibel instability, the characteristic behavior of the rapid magnetic energy growth is analyzed and compared to the analytical estimates for the Weibel instability, given in equations (3.12) and (3.13), for a simulation corresponding to a slightly modified version of the $k_{0,e} = 2\pi/L_0$ case. This simulation used a force factor of $C_f = 1$, and the simulation time was chosen as $t_{\mathrm{max}} = 0.062\, t_{\mathrm{turnover}}$ — significantly shorter than that of the standard case to focus on timescales characteristic to the rapid energy evolution. The initial magnetic field noise amplitude was set to be homogeneous over the 32 lowest Fourier modes, instead of the default 4 lowest. This was done to avoid an initial dependence on wave number in the magnetic energy spectrum, which would make it more difficult to identify the most unstable mode from the time evolution of the spectrum, needed for comparison to the most unstable mode of the Weibel instability.

The magnetic energy evolution obtained in this simulation is shown in figure 5.2a, and the expected rapid growth is clearly present also in this modified version of the

$k_{0,e} = 2\pi/L_0$ case. It will turn out that the timescale of the growth, $\sim 0.01\,t_{\text{turnover}}$, is of the same order of magnitude as the characteristic electron Weibel instability timescale $\gamma_{\text{w},e}^{-1}$, defined according to equation (3.12), calculated for the time point in the middle of the growth phase marked with a star in figure 5.2a. In figure 5.2b the magnetic energy spectrum $E_B(k)$, normalized to the value of the energy spectrum at $k = k_0$ and $t = 0$, is illustrated with each curve corresponding to a time point in the range $t \in [0,\, 0.02\,t_{\text{turnover}}]$. This time range coincides with the pre-saturation phase of the magnetic energy evolution in figure 5.2a. From the time evolution of the spectrum it is apparent that the initial decay of magnetic energy in figure 5.2a corresponds to the quick decay of magnetic energy at high wave numbers. This could be expected from the results of the magnetic field damping simulations in section 4.2.2, where the magnetic field decay rate was found to scale strongly with the spatial wave number. For modes $k/k_0 \gtrsim 5$ the energy spectrum rapidly starts to show the dependence $E_B(k) \sim k^{-8}$, as seen by comparing the slope of the spectra after $t = 0$ to the steep dotted black line in figure 5.2b.

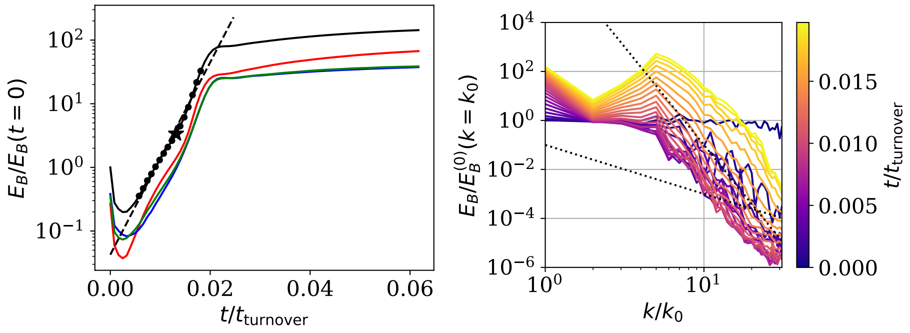

(a) **(b)**

Figure 5.2: The variation of the $k_{0,e} = 2\pi/L_0$ case used in the Weibel instability analysis, which is initiated with homogeneous noise in the magnetic field over the lowest 32 modes. (a) Time evolution of the total magnetic energy (solid black), and the contributions to the energy from the three magnetic field components B_x, B_y, B_z (solid red, blue and green). t_{w} is marked with a star, the other points used for line fitting are marked with dots, and the line fit is shown in dashed black. (b) The magnetic energy spectrum normalized to $E_B(k = k_0,\, t = 0)$, where the curves correspond to each time point in the range $t/t_{\text{turnover}} \in [0,\, 0.02]$ and their color represents the time. Shown in dotted black are k^{-2} and k^{-8}, for reference.

For the Weibel analysis a time point located approximately in the middle of the growth phase is chosen, at $t_{\text{w}} = 0.013\,t_{\text{turnover}}$, marked with a star in figure 5.2a. 16 time steps in the growth phase surrounding the chosen point, corresponding to the time range $t/t_{\text{turnover}} = [0.0058,\, 0.0181]$ and marked with dots in figure 5.2a, are used to estimate the value of the magnetic field growth rate γ. This was done by fitting a linear function to $\ln(E_B/E_B(t=0))$ and defining the obtained slope as 2γ. The obtained fit is shown in dashed black in figure 5.2a, and the growth rate was determined to be $\gamma = 3.32 \cdot 10^{12}\,\text{s}^{-1}$. Studying figure 5.2a closely, the rapid magnetic energy growth is seen to be slightly super-exponential, which is expected of growth due to the Weibel instability in this phase [7], since the anisotropy $\varDelta_e$ is increasing with time because of the sheared flow. The growth rate γ obtained from the linear fit is therefore not exact, but is still seen to represent the actual growth rate quite accurately during most of the rapid growth phase in figure 5.2a.

The mode that appears dominant when studying the magnetic energy spectrum in figure 5.2b, is $5k_0 = 10\pi/L_0$. However, because of the rapid initial decay of magnetic energy at high wave numbers it is somewhat unclear which mode shows the fastest growth, and would be considered the most unstable, since wave numbers higher than $5k_0$ grow by about the same orders of magnitude. As there is no other obvious peak in the spectrum among the wave numbers with large growth, $k_{\text{dom}} = 5k_0 = 1.29 \cdot 10^6\,\text{m}^{-1}$ is chosen as a representative value for the most unstable mode.

The analytical Weibel estimates for the magnetic field strength growth rate $\gamma_{\text{w},\alpha}$ and most unstable mode $k_{\text{w},\alpha}$, defined in equations (3.12) and (3.13) respectively, were calculated from the simulation data using the root-mean-square (RMS) values of d_α and $v_{\text{th},\alpha}$ at that time point (using the $v_{\text{th},\alpha} = \sqrt{T_\alpha/n_\alpha}$ convention). The mean corresponds to an average over the simulation box.

A comparison can be made between the calculated values for the growth rate γ and the most unstable mode k_{dom} to their electron Weibel estimate counterparts at the chosen time t_{w}. At this time the (non-magnetized) electron pressure anisotropy, defined using the RMS-value of $p_{e,max}/p_{e,min}$ in equation (2.15), was $\varDelta_e \approx 0.066$. The ratios of the calculated electron Weibel estimates to the directly obtained growth rate and most unstable mode respectively were in this case:

$$\frac{\gamma}{\gamma_{\text{w},e}} \approx 0.5161 \qquad \frac{k_{\text{dom}}}{k_{\text{w},e}} \approx 0.1761.$$

It is therefore found that the observed growth rate, as well as the wave number corresponding to the peak of the magnetic energy spectrum, are comparable to, but slightly lower than, what the analytical theory of the electron Weibel instability would suggest. The fact that the dominant mode is lower than the corresponding Weibel estimate means that the characteristic spatial scales of the magnetic field are slightly larger than what is expected for the Weibel instability. It is seen that the observed growth rate coincides more closely with the Weibel estimate than the dominant wave number does.

The peak in the magnetic energy spectrum being at a lower wave number than expected is most likely due to the very strong increase of the magnetic field damping towards higher wave numbers, as found in section 4.2.2. Since the Weibel estimate for the growth rate is defined as corresponding to the most unstable mode, other modes, like the one found to dominate here, would have slightly lower growth rates, which is also what is observed. Furthermore, the definition of $\varDelta_e$ given in equation (2.15), where $p_{e,max}$ is the largest eigenvalue and $p_{e,min}$ is the average of the two smallest eigenvalues of the electron pressure tensor, implicitly assumes that the two smallest eigenvalues should be similar, while $p_{e,max}$ should be significantly different from these. This would indicate that the eigenvector corresponding to $p_{e,max}$ is the "preferred direction" of the anisotropy, like how the reference direction for pressure anisotropy in the magnetized regime is along $\boldsymbol{B}$. Studying the actual obtained eigenvalues of the electron pressure tensor, however, the largest and smallest are typically separated by similar amounts from the central one. The fact that there does not seem to be a clear "preferred direction" of the pressure anisotropy, and therefore that the definition of $\mathit{\Delta}_e$ can be interpreted as slightly misleading, could be a contributing factor for why the observed growth rate and dominant mode are not a closer match for the Weibel estimates, that are calculated using $\mathit{\Delta}_e$.

An additional possibility for why k_{dom} differs from what is expected, could be that the most unstable mode expected of the electron Weibel instability at the time t_{w} is estimated to be $k_{\mathrm{w},e} \approx 28k_0$, which is relatively close to what can be resolved on the employed spatial grid. It is therefore conceivable that the limited spatial resolution does not entirely resolve the full effects of the Weibel instability. To investigate this further, higher resolution simulations of the cases presented in figures 5.1 and 5.2 should be performed, given access to sufficient computational resources.

To investigate the possibility of the magnetic energy growth being due to the ion Weibel instability instead, the ion Weibel estimates $\gamma_{\mathrm{w},i}$ and $k_{\mathrm{w},i}$ were calculated in the same manner as for electrons at time t_{w}, but now using ion quantities d_i and $v_{\mathrm{th},i}$. The corresponding ion pressure anisotropy was calculated to be $\mathit{\Delta}_i \approx 0.052$, which results in the ratios:

$$\frac{\gamma}{\gamma_{\mathrm{w},i}} \approx 72.98 \qquad \frac{k_{\mathrm{dom}}}{k_{\mathrm{w},i}} \approx 1.976.$$

While the most unstable mode for the ion Weibel instability, $k_{\mathrm{w},i}$, appears to coincide slightly better with k_{dom} than $k_{\mathrm{w},e}$, the growth rate expected of the ion Weibel instability is significantly smaller than the growth rate observed in the simulation — differing by almost two orders of magnitude. This indicates that the likely dominating Weibel instability during the magnetic field growth is that of the electrons.

This conclusion can be further supported by considering the time evolution of the pressure anisotropy measures $\mathit{\Delta}_e$ and $\mathit{\Delta}_i$, both calculated according to equation (2.15) with the RMS-values of $p_{\alpha,\mathrm{max}}/p_{\alpha,\mathrm{min}}$ (with the mean being a simulation box average). The evolution of these quantities is shown in figure 5.3. Around the time $t = 0.02\,t_{\mathrm{turnover}}$, where the magnetic energy growth saturates in figure 5.2a, the electron pressure anisotropy is decreasing rapidly to a lower value, while the ion anisotropy shows no significant change. This leads to the ion pressure anisotropy overtaking that of the electrons around this time. The fact that a rapid change in $\mathit{\Delta}_e$, which results in $\mathit{\Delta}_i$ starting to dominate, coincides with the saturation of the magnetic energy growth indicates that the growth rate γ depends significantly on $\mathit{\Delta}_e$. Since $\mathit{\Delta}_e$ in turn is a governing quantity of the electron Weibel instability, it implies that this instability could very well be the cause of the rapid magnetic energy growth observed in the simulation.

In [7], the Weibel seed generation stage of the magnetization of a collisionless pair-plasma, in the presence a sheared flow, is studied kinetically. The evolution of the magnetic energy E_B and electron pressure anisotropy $\mathit{\Delta}_e$ found here, in figures 5.2a and 5.3 respectively, is qualitatively similar to the evolution of β^{-1} (essentially the

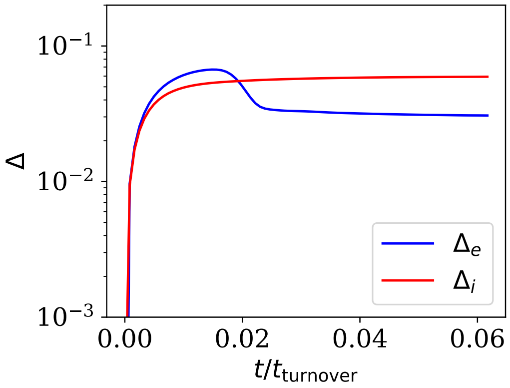

Figure 5.3: Time evolution of the pressure anisotropy measures $\mathit{\Delta}_e$ and $\mathit{\Delta}_i$ for the case used in the Weibel instability analysis.

magnetic energy normalized to the scalar pressure) and $\mathit{\Delta}$ (defined in the same way as $\mathit{\Delta}_e$ here) shown in figure 2 of [7]. Since the rapid magnetic field growth observed in [7] is determined to be caused by the electron Weibel instability, this further reinforces the conclusion that the same holds true for the case presented here.

As previously stated the saturation of E_B that occurs around $t = 0.02\,t_{\text{turnover}}$ in figure 5.2a seems to correspond to the drop in $\mathit{\Delta}_e$ observed in figure 5.3. As discussed in [7] it is expected that the Weibel instability saturates when the increasing magnetization causes the Larmor radius to become comparable to the characteristic length scale of the magnetic field: $r_{\text{L}} k_{\text{w}}^{-1} \sim 1$, or alternatively $r_{\text{L}} k_{\text{dom}}^{-1} \sim 1$. The RMS-value of the Larmor radius for electrons and ions was calculated at the time $t_{\text{sat}} \approx 0.022\,t_{\text{turnover}}$, shortly after saturation. Comparing the Larmor radii to the values of $k_{\text{dom}}^{-1} = (5k_0)^{-1}$ and $k_{\text{w},\alpha}^{-1}$ for electrons and ions, the following values are obtained:

$$\begin{aligned} k_{\text{w},e} r_{\text{L},e} &\approx 13.60 \qquad & k_{\text{dom}} r_{\text{L},e} &\approx 3.163 \\ k_{\text{w},i} r_{\text{L},i} &\approx 16.53 \qquad & k_{\text{dom}} r_{\text{L},i} &\approx 31.64. \end{aligned}$$

At this time $\mathit{\Delta}_e \approx 0.0378$ and $\mathit{\Delta}_i \approx 0.0559$. From this comparison it is seen that while $r_{\text{L},\alpha}$ are not directly comparable to the Weibel estimates $k_{\text{w},\alpha}^{-1}$, the electron Larmor radius has indeed become comparable to the spatial scale $k_{\text{dom}}^{-1} = (5k_0)^{-1}$, corresponding to the dominant mode found in the simulation.

The Weibel instability is usually characterized by filament structures of physical quantities like the magnetic field strength B. Both B and the magnitude of the current density j are plotted at the time t_{w}, for slices of the simulation box at $x, y, z = 0.492L_0$, to investigate whether such structures can be observed. These plots are shown in figures 5.4 and 5.5 respectively, and it can be seen that some relatively small-scale filament structures are present.

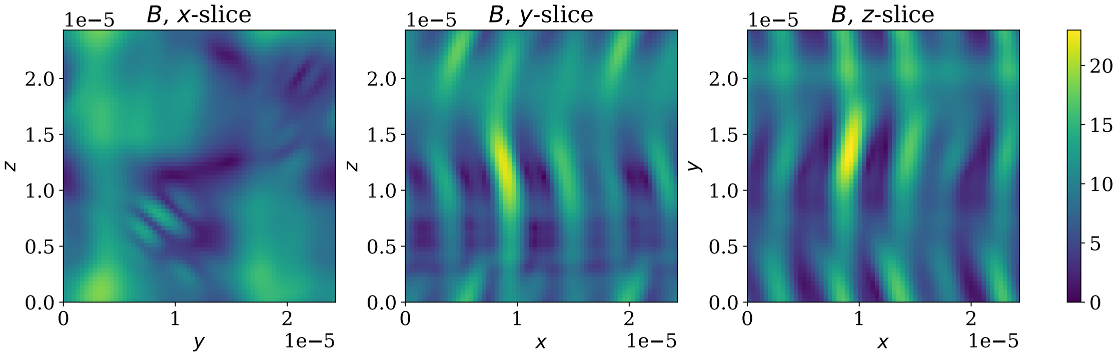

Figure 5.4: The magnetic field strength B in Tesla at time $t_\mathrm{w} = 0.013\, t_\mathrm{turnover}$, in slices of the simulation box at $x, y, z = 0.492 L_0$, for the case used in the Weibel instability analysis.

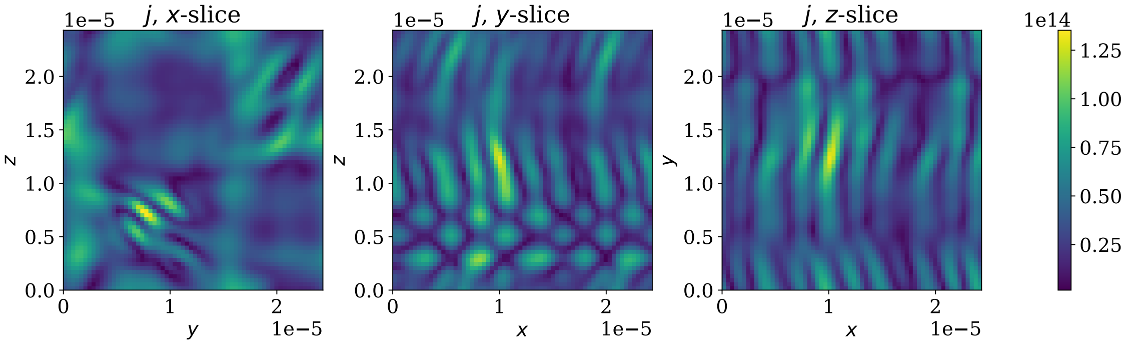

Figure 5.5: The magnitude of the current density j in A/m^2 at time $t_\mathrm{w} = 0.013\, t_\mathrm{turnover}$, in slices of the simulation box at $x, y, z = 0.492 L_0$, for the case used in the Weibel instability analysis.

5.3 Results and Discussion of Dynamo Simulations

All the eight simulations in the scan over the electron closure parameter $k_{0,e}$ were performed and the output analyzed with respect to the magnetic energy, flow energy and magnetic energy spectrum in the same way as in figure 5.1. The results for four representative cases of the scan, $k_{0,e} = 2\pi/(2^{-m} L_0)$ with $m = 0, 3, 5, 7$, are shown in figures 5.1 and 5.6–5.8. The remaining cases whose results are not shown displayed similar features to the cases shown with the closest smaller and larger $k_{0,e}$ value, and followed the same trends.

A general observation for all cases is that the contributions to the flow energy from the y- and z-components of the flow velocity are small compared to the contribution to the total from the x-component. This is a problem inherent to the GP-flow when choosing $A = C$ in equation (3.4), since the RMS-value of the x-component is then always a factor of $\sqrt{2}$ larger than the RMS-values of the other components

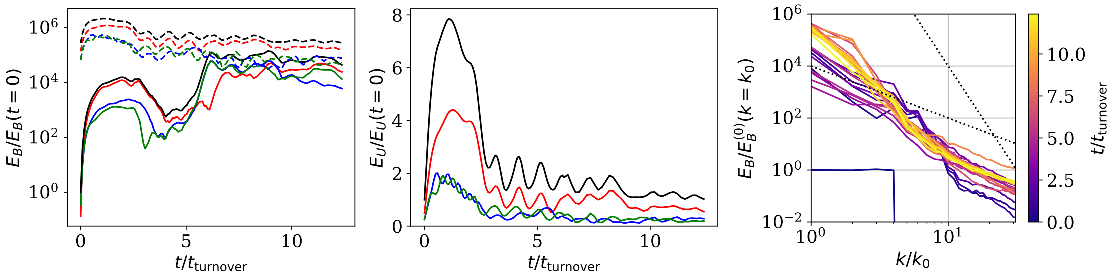

(a) **(b)** **(c)**

Figure 5.6: The $k_{0,e} = 2\pi/(L_0/8)$ case of the electron closure parameter scan. (a) Time evolution of the magnetic energy (solid) and the flow energy (dashed), both normalized to the magnetic energy at $t = 0$. The total energies are shown in black, and the contributions to the energy from the three vector components in the x, y, z-directions are shown in red, blue and green respectively. (b) The total flow energy (black), and its contribution from the three vector components in the x, y, z-directions (red, blue, green), all normalized to its initial value. (c) The magnetic energy spectrum normalized to its value at $k = k_0$ and $t = 0$, for 25 time points approximately uniformly distributed in the range $t/t_{\rm turnover} \in [0, t_{\rm max}]$, where the curve color corresponds to the time. Shown in dotted black are k^{-2} and k^{-8}, for reference.

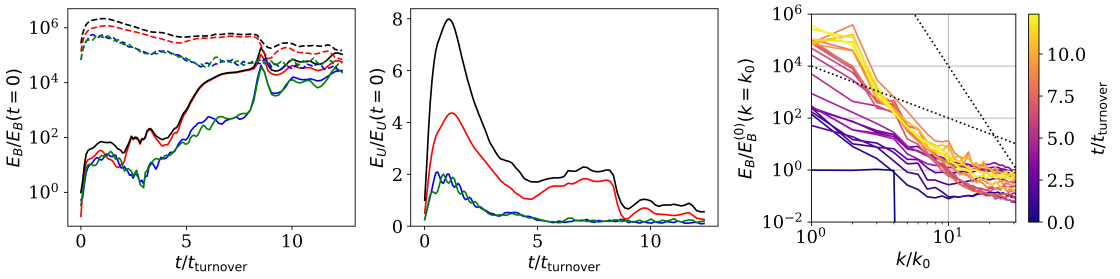

(a) **(b)** **(c)**

Figure 5.7: The $k_{0,e} = 2\pi/(L_0/32)$ case of the electron closure parameter scan. (a) Time evolution of the magnetic energy (solid) and the flow energy (dashed), both normalized to the magnetic energy at $t = 0$. The total energies are shown in black, and the contributions to the energy from the three vector components in the x, y, z-directions are shown in red, blue and green respectively. (b) The total flow energy (black), and its contribution from the three vector components in the x, y, z-directions (red, blue, green), all normalized to its initial value. (c) The magnetic energy spectrum normalized to its value at $k = k_0$ and $t = 0$, for 25 time points approximately uniformly distributed in the range $t/t_{\rm turnover} \in [0, t_{\rm max}]$, where the curve color corresponds to the time. Shown in dotted black are k^{-2} and k^{-8}, for reference.

(where the mean corresponds to an average over the simulation box of side length L_0). Considering that the forcing is done proportional to the GP-flow according to equation (5.2), the x-component of the flow velocity for each species is also

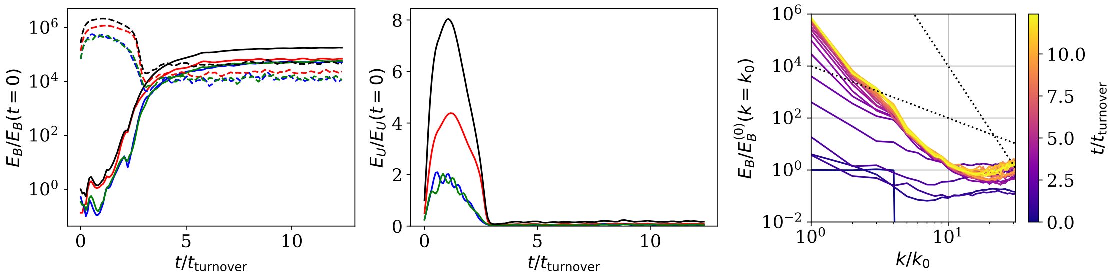

(a) **(b)** **(c)**

Figure 5.8: The $k_{0,e} = 2\pi/(L_0/128)$ case of the electron closure parameter scan. (a) Time evolution of the magnetic energy (solid) and the flow energy (dashed), both normalized to the magnetic energy at $t = 0$. The total energies are shown in black, and the contributions to the energy from the three vector components in the x, y, z-directions are shown in red, blue and green respectively. (b) The total flow energy (black), and its contribution from the three vector components in the x, y, z-directions (red, blue, green), all normalized to its initial value. (c) The magnetic energy spectrum normalized to its value at $k = k_0$ and $t = 0$, for 25 time points approximately uniformly distributed in the range $t/t_{\mathrm{turnover}} \in [0, t_{\max}]$, where the curve color corresponds to the time. Shown in dotted black are k^{-2} and k^{-8}, for reference.

accelerated more on average than the other components, which further explains the uneven contributions of the flow velocity components to the total flow energy. The flow energy from the y- and z-components reaching negligible values compared to the total energy would mean that the flow has essentially died out in these directions, and therefore can not effectively contribute to the three-dimensional nature of the flow necessary to drive a dynamo.

An issue arising from this is that large forcing, and more specifically large force factors, are required in the simulations to keep the flow from dying out in the y- and z-directions. Here a value of $C_f = 2$ was used for the scan, after initial attempts with $C_f = 1$, from which it could be concluded that the forcing was not sufficient to effectively drive a dynamo. Using large forcing of the fluid velocities can, however, lead to the flow becoming sonic some time during the simulation. As illustrated in figures 5.1b and 5.6b–5.8b, the flow energy reaches high values in an initial peak around $t \simeq t_{\mathrm{turnover}}$, and the flow could become sonic at this point. Sonic flows can lead to the development of shocks, which are numerically challenging, as they for example require the resolution of small spatial scales. The effect of shocks in supersonic MHD dynamo simulations is for example studied in [52].

Studying the flow energy in figures 5.1b and 5.6b, some oscillations of the energy can be observed with an approximate period of one turnover time. This is reasonable considering that the forcing is proportional to a GP-flow varying sinusoidally in time with the angular frequency $2\pi/t_{\mathrm{turnover}}$. It can however be noted that such oscillations have nearly disappeared for cases with higher $k_{0,e}$-values, such as in figure 5.7b and 5.8b.

For all cases in the scan over the electron closure parameter, except the very last one corresponding to $k_{0,e} = 2\pi/(L_0/128)$, the magnetic energy shows some rapid initial growth, as is seen in figures 5.1a, 5.6a and 5.7a. This effect grows weaker with increasing $k_{0,e}$ — the magnetic energy reaches smaller and smaller values in this phase. Recalling the form of the isotropization closure, defined in equation (3.14), the closure term increases in size with increasing values of $k_{0,e}$. This would correspond to a stronger isotropization of the pressure tensor for large $k_{0,e}$, not allowing for large pressure anisotropies to develop. As discussed in section 5.2, the early rapid magnetic energy growth is likely associated with the electron Weibel instability, which is driven by electron pressure anisotropy. Consequently, the trend observed of a decreasingly large early rapid magnetic energy growth with increasing $k_{0,e}$ is completely reasonable, and further supports that this growth is indeed associated with the pressure anisotropy-driven Weibel instability.

Studying the evolution of the magnetic energy in figures 5.1a and 5.6a–5.8a it can be noted that while the effects of the Weibel instability decrease with increasing $k_{0,e}$, behavior of the magnetic energy associated with the classical dynamo becomes more apparent. The timescales associated with dynamo growth are on the order of a few turnover times, and saturation of the magnetic energy growth usually occurs once it reaches equipartition with the kinetic energy in the flows. This type of behavior is clearly observed in figure 5.8a, corresponding to the highest value of $k_{0,e}$. The $k_{0,e} = 2\pi/(L_0/64)$ case, not shown here, displayed very similar behavior to that of the $k_{0,e} = 2\pi/(L_0/128)$ case shown in figure 5.8a, but with a slightly smaller growth rate of the magnetic energy before saturation. The $k_{0,e} = 2\pi/(L_0/32)$ case, shown in figure 5.7a, also has a growth rate smaller than that of the $k_{0,e} = 2\pi/(L_0/64)$ case. An increasing dynamo growth rate with $k_{0,e}$ can be expected in this case. The fact that the decay rate of the magnetic field, a consequence of an effective resistivity in the collisionless system, was found in section 4.2.2 to vary as $\gamma_B \sim k_{0,e}^{-1}$, means that the generalized magnetic Reynolds number should vary as $Rm \sim k_{0,e}$ according to equation (3.9). Previous investigations of dynamos using MHD simulations indicate that dynamo growth rate increases with Rm and eventually saturates [53], which in this case would be reflected by the dynamo growth rate increasing with the closure parameter $k_{0,e}$ — just as is observed here when dynamo behavior starts to dominate over the Weibel magnetic field seed generation.

From these observations it can be concluded that low values of the closure parameter $k_{0,e}$, reflecting a small pressure isotropization, or a weak effective collisionality, compares well to the results of kinetic simulations of pair-plasmas, where the Weibel instability is active [5]. On the other hand, high $k_{0,e}$-values, for which the isotropization of the pressure tensor is large — which could be viewed as a strong effective collisionality — reflect classical MHD-like dynamo behavior. This is a reasonable finding, considering that the MHD dynamo treatment assumes a high collisionality of the system. One could then naively assume that setting $k_{0,e} = 0$, effectively removing the heat flux tensor from the 10-moment equations, would be the best way of approaching the results of kinetic simulations. However, having no heat flux effects in the equations is not reasonable either. There is also the issue of the kinetic simulations in question being of pair-plasmas, with a species mass-ratio of 1. An investigation into potential effects of the mass-ratio in the dynamo simulations has not yet been undertaken, but would be an interesting step toward connecting the results of the fluid simulations presented here, and the effect of the closure parameter, with the results of kinetic dynamo simulations of pair-plasmas.

The magnetic energy spectra initially show an almost homogeneous distribution with k for high $k_{0,e}$-values, such as in figure 5.8c. When the energy grows for this case, and the case shown in 5.7c, it does so preferably at small k, or large spatial scales. This leads to a somewhat steep slope developing for small to medium wave numbers. However, there is also some pileup of energy at the highest wave numbers, or smallest spatial scales, reflected in the flatness of the spectrum for these k. This could be an indication of numerical effects (such as positivity preserving flux-limiters) being active at the grid scale. To investigate whether this is the case and if so, to mitigate such numerical artifacts, would require higher resolution simulations, which requires significantly increased computational resources and is thus left outside the scope of this thesis. For lower values of $k_{0,e}$, as in figures 5.1c and 5.6c, the spectrum looks qualitatively different initially. Because of the rapid magnetic energy growth associated with the Weibel instability at the start of the simulation, the spectra have already grown significantly after the first time step. The Weibel growth is similar for low to medium wavenumbers, resulting in close to flat spectra below $k/k_0 \simeq 5$, while there is a larger slope for the higher wave numbers, for early time points. In figure 5.8c there is with time some decay of energy at medium to high wave numbers, and some energy growth at small k, which means that the typical magnetic field spatial scale grows with time. A similar trend is observed in figure 5.6c, but at the largest wave numbers there is some energy growth with time instead.

Because the spectra in figures 5.1c and 5.6c–5.8c generally do not have large ranges of wave numbers where the slope of the spectrum is constant, it is difficult to identify clear power-law behaviors. It is therefore not motivated to fit linear functions to the spectra as one would usually do to find a power-law dependence.

In figures 5.8a and 5.8b, depicting the $k_{0,e} = 2\pi/(L_0/128)$ case, there is a significant quenching of the flow around $t \simeq 2.7\, t_{\text{turnover}}$ where the flow energy decreases by around two orders of magnitude. The magnetic energy also levels off close to this lower energy level. Similar behavior of the flow and magnetic energies was observed in the $k_{0,e} = 2\pi/(L_0/64)$ case as well. This sudden quenching of the flow was not expected, especially considering the strong forcing employed here. An attempt was made to investigate the cause of this flow quenching by studying the output quantity $m_i n_i \boldsymbol{u}_i$ from the 10-moment solver of `Gkeyll`, since the ion fluid velocity is the largest contributor to the MHD mass flow $\boldsymbol{U}$. In figure 5.9, a few time steps in the flow quenching phase are plotted of $m_i n_i u_{i,x}$ for a slice of the simulation box in the x-direction. Notably, the flow quenching starts on the grid scale and then spreads as the maxima and minima of the momentum density rotate slightly in the plane with time. Around $t = 2.72\, t_{\text{turnover}}$ the grid-scale points where the quenching originated have spread to make up a larger region of the plane, increasing the affected spatial scales. The momentum density in the entire plane has also already started decreasing significantly at this point.

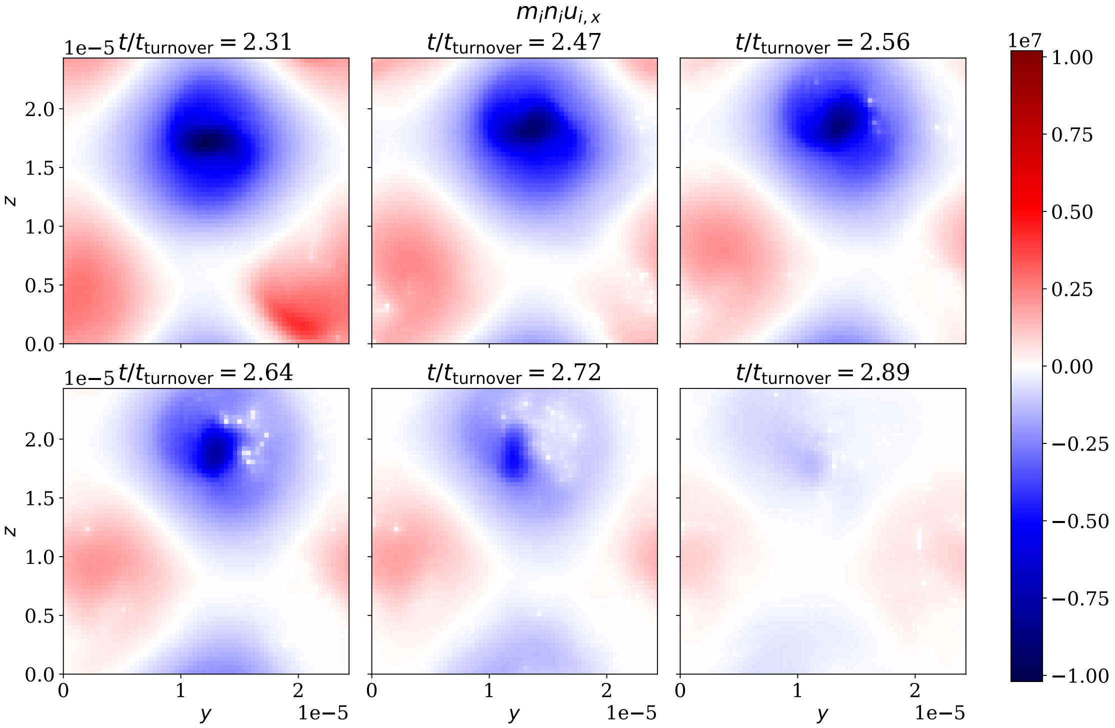

Figure 5.9: Timestamps of $m_i n_i u_{i,x}$ for a slice of the simulation box at the first grid point in x ($x = \Delta x/2$) during the flow quenching in the $k_{0,e} = 2\pi/(L_0/128)$ case, where the color indicates the momentum density values in units of kg/(m^{2}s).

Exactly what the observed grid-scale effects driving the flow quenching are is still an open question. Likely, this is a consequence of numerical issues in the simulation that will need to be investigated further. The appearance of strong flow quenching like that seen in figure 5.8b, in simulations where the flow possibly reaches sonic speeds, may indicate that perhaps the appearance of shocks triggers some numerical response in the simulation that acts as some enormous viscosity. However, it is interesting that the mass flow is otherwise mostly sensitive to $k_{0,i}$, as seen in section 4.2.1, but here the issue appears when setting $k_{0,e}$ to a high value.

6

Conclusions

A still unresolved problem in astrophysics is the origin and evolution of the cosmic magnetization that affects a wide variety of astrophysical systems, which are usually weakly collisional. The dynamo process, which is thought to sustain and have amplified observed astrophysical magnetic fields, has classically been treated using the MHD description, that is not valid in the collisionless regime. Combined with the kinetic nature of possible magnetic field seed generation mechanisms like the Weibel instability, this motivates treating the cosmic magnetization problem with more advanced plasma models. Collisionless fluid models constitute a promising option, since a fully kinetic treatment of magnetic field growth in proton-electron plasmas would require unreasonably large computational resources. In this thesis, magnetic field growth in collisionless plasmas has been studied through simulations with driven turbulent flows, using the collisionless 10-moment fluid model of the `Gkeyll` simulation tool, which evolves the full pressure tensor for both ions and electrons.

The strength of the heat flux closures available for the collisionless fluid model, the isotropization closure and the gradient-based closure, could be adjusted with the free closure parameters $k_{0,e}$ and $k_{0,i}$ for the electrons and ions respectively. The magnetic and fluid Reynolds numbers set the scale separation between energy injection and dissipation scales of magnetic fields and mass flows, and they play an important role in MHD dynamo theory. Lacking explicit resistivity and viscosity in the collisionless systems studied here, these dimensionless numbers were generalized to apply for a collisionless system by studying the dependencies of the flow and magnetic field strength decay rates on the closure parameters. In simple one-dimensional non-driven simulations of spatially sinusoidal flows or magnetic fields, with wave number k_x, using the isotropization closure, the flow decay rate was found to scale approximately as $k_x^2/k_{0,i}$, while the magnetic field damping rate is approximately proportional to $k_x^4/k_{0,e}$. The scaling $\gamma_B \sim k_x^4$ was shown to become increasingly more accurate with increasing mass-ratio, so the same can be assumed for the other dependencies of γ_B and γ_U as well. The generalized magnetic and fluid Reynolds numbers are inversely proportional to the magnetic field and flow decay rates, respectively, which means that the magnetic Reynolds number was found to be approximately proportional to $k_{0,e}$ and the fluid Reynolds number approximately proportional to $k_{0,i}$ for the isotropization closure.

Using the gradient-based closure did not result in a simple exponential decay of the flow or magnetic field, but demonstrated both oscillatory behavior and mode decay of the wave number characteristic to the initial sinusoidal spatial variation of the flow or field. It was therefore concluded that the results with the gradient-based closure were physically questionable, and that the closure might not be well-suited to the problem, which motivated only using the isotropization closure in the subsequent dynamo simulations.

The fact that the flow and magnetic field decay rates were found in the damping simulations using the isotropization closure to be essentially independent of the electron and ion closure parameters respectively, indicates that the ion-electron mass-ratio used is sufficiently large for a decoupling of the electron and ion dynamics, making it possible to investigate physics beyond that of pair-plasmas in the following dynamo simulations. Further confirmation of this decoupling was achieved by deriving theoretically an expression for the ion flow damping rate, and noting that this and the MHD flow damping rate are consistent with respect to their dependencies on the closure parameters and the wave number characteristic to the sinusoidal flow.

Three-dimensional dynamo simulations were performed for a range of values of the electron closure parameter, which determines the strength of the electron pressure isotropization, corresponding to a scan over the effective magnetic Reynolds number. Both magnetic field growth from the dynamo process and magnetic field seed generation from the pressure anisotropy-driven Weibel instability were observed in the simulations. Using a collisionless fluid model, instead of MHD or kinetic descriptions, therefore allows studying both magnetic field seed generation through instabilities and the full dynamo growth to saturation, two processes characterized by vastly different spatial and temporal scales, at a finite ion-electron mass-ratio.

For a weak electron pressure isotropization, corresponding to a small effective magnetic Reynolds number and weak effective collisionality, seed generation from the electron Weibel instability dominates the magnetic field growth. A qualitative similarity was observed between the magnetic and flow energy evolution in this case and that observed in previous kinetic studies of dynamos in pair-plasmas [5], where the cause of the rapid energy growth observed was determined to be the Weibel instability. The magnetic field growth rate and dominant Fourier mode of the magnetic energy spectrum obtained from the dynamo simulations were shown to be comparable to the corresponding analytical predictions for the electron Weibel instability, as given by [7]. The rapid magnetic field growth was also shown to correlate to the growth of the electron pressure anisotropy, and saturation occurred approximately when the electrons became magnetized, both behaviors expected of the electron Weibel instability [7], which strengthens the conclusion that this is the cause of the rapid magnetic field growth.

As expected, the effect of the Weibel instability was seen to decrease with increasing strength of the electron closure, corresponding to an increasing pressure isotropization, since it is pressure anisotropy-driven. In the limit of strong pressure isotropization from the closure, corresponding to a high magnetic Reynolds number and strong effective collisionality, typical MHD-like dynamo behavior of the magnetic field growth dominates over seed generation. The dynamo growth timescales were on the order of turnover times of the driven turbulent flow, and the growth rate was seen to increase with the effective magnetic Reynolds number, also in accordance with MHD studies of dynamos [53].

To take the work done in this thesis further, the flow quenching for high pressure isotropization strengths, observed when the magnetic field growth saturates in the dynamo simulations, needs to be thoroughly investigated. There is a possibility that grid-scale numerical artifacts in the simulation are the cause, so performing the corresponding simulations at a higher spatial resolution would therefore be a useful test. Some preliminary results from dynamo simulations at higher resolution, not presented in this thesis, indicate that there is some dependence of the results on the resolution. However, noting that the computational expense of the simulations grows with the fourth power of the linear resolution, the limited computational resources of this project did not allow for performing an entire scan over the effective magnetic Reynolds number at a resolution larger than the one employed here. The whole range of dynamo simulations should, however, be repeated using a higher spatial resolution, given the access to sufficient computational resources.

Finally, an interesting avenue to pursue to build on the results presented in this thesis would be to investigate the effect that the chosen ion-electron mass-ratio has on the dynamo simulations. Studying dynamo simulations employing a range of mass-ratios starting from the value 1, corresponding to a pair-plasma, would make it possible to properly connect the results of the fluid dynamo simulations to the results of kinetic dynamo simulations of pair-plasmas [5], where a higher mass-ratio cannot be employed due to the immense additional computational cost.

Bibliography

[1] F. Rincon, "Dynamo Theories," *Journal of Plasma Physics*, vol. 85, no. 4, p. 205 850 401, 2019. DOI: 10.1017/S0022377819000539.

[2] A. Brandenburg and K. Subramanian, "Astrophysical Magnetic Fields and Nonlinear Dynamo Theory," *Physics Reports*, vol. 417, no. 1, pp. 1–209, 2005. DOI: 10.1016/j.physrep.2005.06.005.

[3] F. Rincon, F. Califano, A. A. Schekochihin, and F. Valentini, "Turbulent Dynamo in a Collisionless Plasma," *Proceedings of the National Academy of Sciences*, vol. 113, no. 15, pp. 3950–3953, 2016. DOI: 10.1073/pnas.1525194113.

[4] D. A. St-Onge and M. W. Kunz, "Fluctuation Dynamo in a Collisionless, Weakly Magnetized Plasma," *The Astrophysical Journal Letters*, vol. 863, no. 2, p. L25, Aug. 2018. DOI: 10.3847/2041-8213/aad638.

[5] M. Zhou, V. Zhdankin, M. W. Kunz, N. F. Loureiro, and D. A. Uzdensky, "Magnetogenesis in a Collisionless Plasma: From Weibel Instability to Turbulent Dynamo," *The Astrophysical Journal*, vol. 960, no. 1, p. 12, Dec. 2023. DOI: 10.3847/1538-4357/ad0b0f.

[6] J. Ng, "Fluid Closures for the Modelling of Reconnection and Instabilities in Magnetotail Current Sheets," Ph.D. dissertation, Department of Astrophysical Sciences, Princeton University, Princeton, USA, 2019. [Online]. Available: http://arks.princeton.edu/ark:/88435/dsp015d86p299f (visited on May 20, 2025).

[7] M. Zhou, V. Zhdankin, M. W. Kunz, N. F. Loureiro, and D. A. Uzdensky, "Spontaneous Magnetization of Collisionless Plasma," *Proceedings of the National Academy of Sciences*, vol. 119, no. 19, e2119831119, 2022. DOI: 10.1073/pnas.2119831119.

[8] Princeton University. "GKEYLL: Overview." (2020), [Online]. Available: https://heliophysics.princeton.edu/gkeyll/overview (visited on May 20, 2025).

[9] A. Hakim and the Gkeyll Team. "The Gkeyll 2.0 Code: Documentation Home." (2024), [Online]. Available: https://gkeyll.readthedocs.io/en/latest (visited on May 20, 2025).

[10] A. Hakim and the Gkeyll Team. "Gkeyll 2.0." GitHub Repository. (2023), [Online]. Available: https://github.com/ammarhakim/gkyl (visited on May 20, 2025).

[11] F. F. Chen, *Introduction to Plasma Physics and Controlled Fusion*, 3rd ed. Cham, Switzerland: Springer International Publishing AG, 2016. DOI: 10.1007/978-3-319-22309-4.

[12] P. M. Bellan, *Fundamentals of Plasma Physics*. Cambridge, England: Cambridge University Press, 2006. DOI: 10.1017/CBO9780511807183.

[13] E. R. Ingelsten, M. C. McGrae-Menge, E. P. Alves, and I. Pusztai, "Data-Driven Discovery of a Heat Flux Closure for Electrostatic Plasma Phenomena," *Journal of Plasma Physics*, vol. 91, no. 2, E64, 2025. DOI: 10.1017/S0022377825000285.

[14] P. Helander, M. Strumik, and A. A. Schekochihin, "Constraints on Dynamo Action in Plasmas," *Journal of Plasma Physics*, vol. 82, no. 6, p. 905 820 601, 2016. DOI: 10.1017/S0022377816000982.

[15] G. F. Chew, M. L. Goldberger, F. E. Low, and S. Chandrasekhar, "The Boltzmann Equation and the One-Fluid Hydromagnetic Equations in the Absence of Particle Collisions," *Proceedings of the Royal Society of London. Series A. Mathematical and Physical Sciences*, vol. 236, no. 1204, pp. 112–118, 1956. DOI: 10.1098/rspa.1956.0116.

[16] T. G. Cowling, "The Magnetic Field of Sunspots," *Monthly Notices of the Royal Astronomical Society*, vol. 94, no. 1, pp. 39–48, Nov. 1933. DOI: 10.1093/mnras/94.1.39.

[17] Y. B. Zel'dovich, "The Magnetic Field in the Two-Dimensional Motion of a Conducting Turbulent Fluid," *Zhurnal Eksperimental'nol i Teoreticheskoz Fiziki*, vol. 31, p. 154, 1956.

[18] Y. B. Zel'dovich, "The Magnetic Field in the Two-Dimensional Motion of a Conducting Turbulent Fluid," *Soviet Journal of Experimental and Theoretical Physics*, vol. 4, p. 460, 1957.

[19] G. O. Roberts, "Spatially Periodic Dynamos," *Philosophical Transactions of the Royal Society of London. Series A, Mathematical and Physical Sciences*, vol. 266, no. 1179, pp. 535–558, 1970. [Online]. Available: http://www.jstor.org/stable/73752 (visited on May 21, 2025).

[20] D. J. Galloway and M. R. E. Proctor, "Numerical Calculations of Fast Dynamos in Smooth Velocity Fields with Realistic Diffusion," *Nature*, vol. 356, no. 6371, pp. 691–693, Apr. 1992. DOI: 10.1038/356691a0.

[21] M. W. Kunz, A. A. Schekochihin, and J. M. Stone, "Firehose and Mirror Instabilities in a Collisionless Shearing Plasma," *Physical Review Letters*, vol. 112, no. 20, p. 205 003, May 2014. DOI: 10.1103/PhysRevLett.112.205003.

[22] L. M. Widrow, D. Ryu, D. R. G. Schleicher, K. Subramanian, C. G. Tsagas, and R. A. Treumann, "The First Magnetic Fields," *Space Science Reviews*, vol. 166, pp. 37–70, May 2012. DOI: 10.1007/s11214-011-9833-5.

[23] R. Durrer and A. Neronov, "Cosmological Magnetic Fields: Their Generation, Evolution and Observation," *The Astronomy and Astrophysics Review*, vol. 21, p. 62, Jun. 2013. DOI: 10.1007/s00159-013-0062-7.

[24] K. Subramanian, "The Origin, Evolution and Signatures of Primordial Magnetic Fields," *Reports on Progress in Physics*, vol. 79, no. 7, p. 076 901, May 2016. DOI: 10.1088/0034-4885/79/7/076901.

[25] A. Seta and C. Federrath, "Seed Magnetic Fields in Turbulent Small-Scale Dynamos," *Monthly Notices of the Royal Astronomical Society*, vol. 499, no. 2, pp. 2076–2086, Sep. 2020. DOI: 10.1093/mnras/staa2978.

[26] K. Subramanian, D. Narasimha, and S. M. Chitre, "Thermal Generation of Cosmological Seed Magnetic Fields in Ionization Fronts," *Monthly Notices of the Royal Astronomical Society*, vol. 271, no. 1, pp. L15–L18, Nov. 1994. DOI: `10.1093/mnras/271.1.L15`.

[27] N. Y. Gnedin, A. Ferrara, and E. G. Zweibel, "Generation of the Primordial Magnetic Fields during Cosmological Reionization," *The Astrophysical Journal*, vol. 539, no. 2, p. 505, Aug. 2000. DOI: `10.1086/309272`.

[28] M. Langer and J.-B. Durrive, "Magnetizing the Cosmic Web during Reionization," *Galaxies*, vol. 6, no. 4, p. 124, 2018. DOI: `10.3390/galaxies6040124`.

[29] R. Kulsrud, S. C. Cowley, A. V. Gruzinov, and R. N. Sudan, "Dynamos and Cosmic Magnetic Fields," *Physics Reports*, vol. 283, no. 1, pp. 213–226, 1997. DOI: `10.1016/S0370-1573(96)00061-0`.

[30] R. M. Kulsrud, R. Cen, J. P. Ostriker, and D. Ryu, "The Protogalactic Origin for Cosmic Magnetic Fields," *The Astrophysical Journal*, vol. 480, no. 2, p. 481, May 1997. DOI: `10.1086/303987`.

[31] G. Davies and L. M. Widrow, "A Possible Mechanism for Generating Galactic Magnetic Fields," *The Astrophysical Journal*, vol. 540, no. 2, p. 755, Sep. 2000. DOI: `10.1086/309358`.

[32] L. Biermann and A. Schlüter, "Über den Ursprung der Magnetfelder auf Sternen und im interstellaren Raum," *Zeitschrift für Naturforschung A*, vol. 5, pp. 65–71, 1950. DOI: `10.1515/zna-1950-0201`.

[33] R. Schlickeiser and P. K. Shukla, "Cosmological Magnetic Field Generation by the Weibel Instability," *The Astrophysical Journal*, vol. 599, no. 2, p. L57, Dec. 2003. DOI: `10.1086/381246`.

[34] I. Pusztai *et al.*, "Dynamo in Weakly Collisional Nonmagnetized Plasmas Impeded by Landau Damping of Magnetic Fields," *Physical Review Letters*, vol. 124, no. 25, p. 255 102, Jun. 2020. DOI: `10.1103/PhysRevLett.124.255102`.

[35] L. Wang, K. Germaschewski, A. Hakim, C. Dong, J. Raeder, and A. Bhattacharjee, "Electron Physics in 3-D Two-Fluid 10-Moment Modeling of Ganymede's Magnetosphere," *Journal of Geophysical Research: Space Physics*, vol. 123, no. 4, pp. 2815–2830, Mar. 2018. DOI: `10.1002/2017JA024761`.

[36] C. Dong *et al.*, "Global Ten-Moment Multifluid Simulations of the Solar Wind Interaction with Mercury: From the Planetary Conducting Core to the Dynamic Magnetosphere," *Geophysical Research Letters*, vol. 46, no. 21, pp. 11 584–11 596, Oct. 2019. DOI: `10.1029/2019GL083180`.

[37] L. Wang, A. H. Hakim, J. Ng, C. Dong, and K. Germaschewski, "Exact and Locally Implicit Source Term Solvers for Multifluid-Maxwell Systems," *Journal of Computational Physics*, vol. 415, p. 109 510, Aug. 2020. DOI: `10.1016/j.jcp.2020.109510`.

[38] S. Jarmak *et al.*, "QUEST: A New Frontiers Uranus Orbiter Mission Concept Study," *Acta Astronautica*, vol. 170, pp. 6–26, May 2020. DOI: `10.1016/j.actaastro.2020.01.030`.

[39] L. Wang, A. H. Hakim, A. Bhattacharjee, and K. Germaschewski, "Comparison of Multi-Fluid Moment Models with Particle-In-Cell Simulations of Colli-

sionless Magnetic Reconnection," *Physics of Plasmas*, vol. 22, no. 1, p. 012 108, Jan. 2015. DOI: 10.1063/1.4906063.

[40] J. Ng *et al.*, "The Island Coalescence Problem: Scaling of Reconnection in Extended Fluid Models Including Higher-Order Moments," *Physics of Plasmas*, vol. 22, no. 11, p. 112 104, Nov. 2015. DOI: 10.1063/1.4935302.

[41] J. Ng, A. Hakim, A. Bhattacharjee, A. Stanier, and W. Daughton, "Simulations of Anti-Parallel Reconnection Using a Nonlocal Heat Flux Closure," *Physics of Plasmas*, vol. 24, no. 8, p. 082 112, Aug. 2017. DOI: 10.1063/1.4993195.

[42] J. Ng, A. Hakim, and A. Bhattacharjee, "Using the Maximum Entropy Distribution to Describe Electrons in Reconnecting Current Sheets," *Physics of Plasmas*, vol. 25, no. 8, p. 082 113, Aug. 2018. DOI: 10.1063/1.5041758.

[43] J. Ng, A. Hakim, J. Juno, and A. Bhattacharjee, "Drift Instabilities in Thin Current Sheets Using a Two-Fluid Model With Pressure Tensor Effects," *Journal of Geophysical Research: Space Physics*, vol. 124, no. 5, pp. 3331–3346, Apr. 2019. DOI: 10.1029/2018JA026313.

[44] J. M. TenBarge, J. Ng, J. Juno, L. Wang, A. H. Hakim, and A. Bhattacharjee, "An Extended MHD Study of the 16 October 2015 MMS Diffusion Region Crossing," *Journal of Geophysical Research: Space Physics*, vol. 124, no. 11, pp. 8474–8487, Sep. 2019. DOI: 10.1029/2019JA026731.

[45] J. Ng, A. Hakim, L. Wang, and A. Bhattacharjee, "An Improved Ten-Moment Closure for Reconnection and Instabilities," *Physics of Plasmas*, vol. 27, no. 8, p. 082 106, Aug. 2020. DOI: 10.1063/5.0012067.

[46] J. Ng, L.-J. Chen, A. Hakim, and A. Bhattacharjee, "Reconstruction of Electron and Ion Distribution Functions in a Magnetotail Reconnection Diffusion Region," *Journal of Geophysical Research: Space Physics*, vol. 125, no. 7, e2020JA027879, May 2020. DOI: 10.1029/2020JA027879.

[47] R. Courant, K. Friedrichs, and H. Lewy, "Über die partiellen Differenzengleichungen der mathematischen Physik," *Mathematische Annalen*, vol. 100, pp. 32–74, 1928. [Online]. Available: http://eudml.org/doc/159283.

[48] R. Courant, K. Friedrichs, and H. Lewy, "On the Partial Difference Equations of Mathematical Physics," *IBM Journal of Research and Development*, vol. 11, no. 2, pp. 215–234, Mar. 1967. DOI: 10.1147/rd.112.0215.

[49] I. Pusztai *et al.*, "Kinetic Dynamo in Non-Magnetized Plasmas Impeded by Magnetic Landau Damping," *47th EPS Conference on Plasma Physics*, 2021, O1.402. [Online]. Available: https://info.fusion.ciemat.es/OCS/EPS2021PAP/pdf/O1.402.pdf (visited on Mar. 5, 2025).

[50] D. D. Ryutov, N. L. Kugland, H. S. Park, C. Plechaty, B. A. Remington, and J. S. Ross, "Basic Scalings for Collisionless-Shock Experiments in a Plasma Without Pre-Imposed Magnetic Field," *Plasma Physics and Controlled Fusion*, vol. 54, no. 10, p. 105 021, Sep. 2012. DOI: 10.1088/0741-3335/54/10/105021.

[51] M. W. Kunz, T. W. Jones, and I. Zhuravleva, "Plasma Physics of the Intracluster Medium," in *Handbook of X-ray and Gamma-ray Astrophysics*, C. Bambi and A. Santangelo, Eds. Singapore: Springer Nature Singapore, 2022, pp. 1–42. DOI: 10.1007/978-981-16-4544-0_125-1.

[52] N. Kriel, J. R. Beattie, C. Federrath, M. R. Krumholz, and J. K. J. Hew, "Fundamental MHD Scales - II. The Kinematic Phase of the Supersonic Small-Scale Dynamo," *Monthly Notices of the Royal Astronomical Society*, vol. 537, no. 3, pp. 2602–2629, Jan. 2025. DOI: `10.1093/mnras/staf188`.

[53] S. M. Tobias, "The Turbulent Dynamo," *Journal of Fluid Mechanics*, vol. 912, P1, Feb. 2021. DOI: `10.1017/jfm.2020.1055`.

A

Derivation of Theoretical Ion Flow Damping Rate

The following is a derivation of the analytical solutions for the ion flow damping rate γ_i, as presented in section 4.2.1.1, equation (4.4). Study the z- and xz-components of the ion momentum and energy equations respectively, under the ansatz

$$\begin{aligned} u_z &= u_{z,0}\exp(-\gamma t)\sin(k_x x) \\ p_{xz} &= p_{xz,0}\exp(-\gamma t)\sin(k_x x-\varphi), \end{aligned} \tag{A.1}$$

where the ion species index has been omitted and $u_{z,0}$ and $p_{xz,0}$ are positive, constant amplitudes. Including only the terms with time derivatives, and the terms that are shown to dominate in section 4.2.1.1, the equations are:

$$mn\frac{\partial u_z}{\partial t}+\frac{\partial p_{xz}}{\partial x}\approx 0 \tag{A.2}$$

$$\frac{\partial p_{xz}}{\partial t}+p_{xx}\frac{\partial u_z}{\partial x}+v_{\mathrm{th}}k_0 p_{xz}\approx 0 \tag{A.3}$$

since any spatial variation is in the x-direction in the situation considered for the 1-dimensional simulations. Using the ansatz (A.1) in equation (A.2) the following result is obtained:

$$\begin{aligned} mn(-\gamma)u_{z,0}\exp(-\gamma t)\sin(k_x x)+p_{xz,0}\exp(-\gamma t)k_x\cos(k_x x-\varphi)=0 \\ \implies p_{xz,0}=\frac{mnu_{z,0}\gamma}{k_x}\frac{\sin(k_x x)}{\cos(k_x x-\varphi)}. \end{aligned} \tag{A.4}$$

Taking n to not vary significantly with x, all x-dependence must cancel in the last fraction. For $\gamma>0$ to be true, it is therefore required that $\cos(k_x x-\varphi)=\sin(k_x x)$, which determines $\varphi=\pi/2$. The result (A.4) then becomes:

$$p_{xz,0}=\frac{mnu_{z,0}\gamma}{k_x}. \tag{A.5}$$

Now using the ansatz (A.1) in equation (A.3), the equation

$$\begin{aligned} p_{xz,0}(-\gamma)\exp(-\gamma t)\sin(k_x x-\varphi)+p_{xx}u_{z,0}\exp(-\gamma t)k_x\cos(k_x x)+ \\ +v_{\mathrm{th}}k_0 p_{xz,0}\exp(-\gamma t)\sin(k_x x-\varphi)=0 \end{aligned} \tag{A.6}$$

is obtained. Using $\sin(k_x x - \varphi) = -\cos(k_x x)$, since $\varphi = \pi/2$, all sinusoidal and exponential factors can be divided away given that a solution is wanted for general x. The result (A.5) can then be inserted into the remaining equation

$$p_{xz,0}\gamma + p_{xx}u_{z,0}k_x - v_{\mathrm{th}}k_0 p_{xz,0} = 0 \tag{A.7}$$

to get:

$$\begin{aligned}
&\frac{mnu_{z,0}}{k_x}\gamma^2 - v_{\mathrm{th}}k_0\frac{mnu_{z,0}}{k_x}\gamma + p_{xx}u_{z,0}k_x = 0\\
\implies &\gamma^2 - v_{\mathrm{th}}k_0\gamma + \frac{k_x^2 p_{xx}}{mn} = 0\\
\implies &\gamma = \frac{v_{\mathrm{th}}k_0}{2}\left(1 \pm \sqrt{1 - \frac{4p_{xx}}{mnv_{\mathrm{th}}^2}\frac{k_x^2}{k_0^2}}\right).
\end{aligned} \tag{A.8}$$

Assuming that $p_{xx} \approx p$, in effect that the system is close to thermodynamic equilibrium, and using $p = nT = mnv_{\mathrm{th}}^2$ in the `Gkeyll` $v_{\mathrm{th}} = \sqrt{T/m}$ convention, this corresponds to:

$$\gamma = \frac{v_{\mathrm{th}}k_0}{2}\left(1 \pm \sqrt{1 - 4\frac{k_x^2}{k_0^2}}\right). \tag{A.9}$$

In the limit $k_0 \gg k_x$, Taylor expanding to first order and reinserting the species index for ions:

$$\gamma_i \approx \frac{v_{\mathrm{th},i}k_{0,i}}{2}\left(1 \pm \left(1 - 2\frac{k_x^2}{k_{0,i}^2}\right)\right) = \begin{cases} v_{\mathrm{th},i}k_{0,i}\left(1 - \frac{k_x^2}{k_{0,i}^2}\right) \\ v_{\mathrm{th},i}\frac{k_x^2}{k_{0,i}} \end{cases}. \tag{A.10}$$

The second solution notably shows the same dependencies for flow decay as those found in section 4.2.1, to the nearest integer exponents of k_x and $k_{0,i}$.

DEPARTMENT OF PHYSICS
CHALMERS UNIVERSITY OF TECHNOLOGY
Gothenburg, Sweden
www.chalmers.se

CHALMERS
UNIVERSITY OF TECHNOLOGY